PHYSICAL REVIEW E **76**, 016302 (2007)

Multiple resonant scattering of water waves by a two-dimensional array of vertical cylinders: Linear aspects

Yile Li[*]
Department of Mechanical Engineering, Massachusetts Institute of Technology, Cambridge, Massachusetts 02139, USA

Chiang C. Mei[†]
Department of Civil & Environmental Engineering, Massachusetts Institute of Technology, Cambridge, Massachusetts 02139, USA

(Received 9 February 2007; published 9 July 2007)

We study the Bragg resonance of surface water waves by a two-dimensional array of vertical cylinders covering a large area of the sea. Starting from the resonance criterion known in the physics of solid state and crystallography, we employ asymptotic techniques to derive two-dimensional coupled-mode equations for the envelopes of scattered waves resonated by a plane incident wave. Explicit analytical solutions are obtained for a long strip of cylinder array which may be used for supporting a future offshore airport. Examples of both two-wave and three-wave resonances are discussed in detail. Roles of the band gaps are examined.

DOI: 10.1103/PhysRevE.76.016302 PACS number(s): 47.90.+a, 42.70.Qs, 47.35.−i, 92.10.Hm

I. INTRODUCTION

As the world's population increases, especially along ocean coasts, use of offshore space is a reality and has been proposed for a variety of future applications. For example, there are now five offshore airports in Japan constructed on artificial islands (Nakasaki, Kansai, Kobe, New Kitakyushu, and Chubu). In deep water, a 1000-m long model of floating airport (called the megafloat) has been tested in Tokyo Bay. For military operations, US Navy has studied the feasibility of mobile offshore bases (MOB) by linking a train of modules with the decks kept above the sea surface by semi-submersibles [1]. In intermediate water depths, a possible type of future offshore airport is a long platform supported above water by an array of vertical cylinders resting rigidly on the seabed, similar to the fixed oil-drilling platforms in sea depths less than 100 m. For material economy, the radius of the cylinders will likely be much smaller than the spacing. For such a structure, theoretical prediction of wave-structure interaction should take into account of the mutual influence of adjacent cylinders.

Wave propagation in periodic media is of course a topic of longstanding interest in several branches of physics, notably crystallography [2], solid-state physics [3,4], optics [5], and photonics [6]. A large part of the interest is on the dispersion relation and band structure for a medium of infinite extent, obtained from the eigensolution of a homogeneous boundary-value problem. In the linearized theory of water waves, similar contributions have been made [7–12].

Diffraction by a periodic medium of finite extent has a rich literature in optics [5,13] and in crystallography [14]. If the size of and the spacing between the scatterers are comparable or arbitrary, solution methods usually require considerable numerical computation. Examples are the *S*-matrix theory which may involve boundary integrals based on Green's functions or methods of finite elements for electromagnetic waves (see [15] for a recent survey). For circular cylinders in water waves, Graf's addition theorem for Bessel functions (see Sec. 11.3 [44] or Eq. 9.1.79 [45]) has been used to expedite the computation of series solution for multiple scattering [16–20]. Many mathematical aspects of these methods can be found in [21] or [22]. For water waves there are approximate methods developed for a number of vertical cylinders spaced at a distance much greater than the wavelength [23–25], or when the wavelength is much greater than both the scatterer dimension and spacing (e.g., [26]).

As in optics and solid-state physics, the case of resonant scattering by a periodic array is of special interest in water-wave dynamics. For one-dimensional Bragg reflection of plane waves by parallel corrugations on the seabed, experiments have shown strong reflection by the Bragg mechanism [27]. For two-dimensional scattering of water waves emanating from a point source on one side of a long strip of cylinder array, the superlensing effect has been demonstrated in experiments and confirmed by a semianalytical theory [28]. In two-dimensional radiation from a point inside an infinite array of holes on the bottom of the water layer, self-collimation is possible [29]. In these studies the density of scatterers is high. Theoretical calculations require some computational labor in order to yield physical insight. For Bragg scattering of optical waves in layered media or wave guides, the one-dimensional *coupled-mode equations* (CME) are effective approximations if the periodic variation of medium properties is weak [5,30,31]. With CME, physical deductions can be made explicitly with little numerical effort. In water-wave theory, similar equations have been derived by the perturbation method of multiple scales, for periodic sand bars on the seabed [32–36]. The technique of multiple scales has also been applied to one-dimensional nonlinear optics [37].

In this article, we consider the diffraction of plane monochromatic incident waves from the open sea by a two-dimensional array of vertical cylinders. The radius of the cylinder is assumed to be much smaller than the incident wavelength. We first derive the *two-dimensional* coupled-mode equations for the mutually resonating wave envelopes

---

[*] Present address: Shell International Exploration & Production Inc., Houston, TX 77025, USA.

[†] ccmei@mit.edu

by an asymptotic analysis for the general case where there can be $N-1$ scattered waves by Bragg resonance. These equations are then used to obtain analytical solutions for scattering by a long strip of cylinder array that simulates the supporting structure of an offshore airport. Explicit analytical results will be given for cases where one or two scattered waves are resonated by a plane incident wave. A variety of scattering configurations will be demonstrated for a range of small frequency detuning in and outside the band gaps.

Although this study addresses a problem in water waves, the theory and results can be readily applied to or modified for other physical problems such as sound waves scattered by rigid cylinders, and horizontally sheared elastic waves scattered by cylindrical cavities in a solid, etc. Extensions to three-dimensional resonant scattering and to second-order nonlinear effects are also conceivable.

II. CONCEPTS FROM CRYSTALLOGRAPHY

We shall employ a few concepts on Bragg resonance in a two-dimensional periodic medium, well known in solid-state physics and crystallography [2–4], but used in water-wave theory only recently.

In the horizontal plane of (x,y), let the cylinder centers define the direct lattice. In terms of the primitive vectors $\mathbf{a}_1$ and $\mathbf{a}_2$ which connect two adjacent lattice points in two different directions, a lattice vector connecting any two lattice points, or nodes, can be expressed as

$$\mathbf{R}(m_1,m_2) = m_1\mathbf{a}_1 + m_2\mathbf{a}_2. \tag{1}$$

where m_1,m_2 are integers. On the other hand, the *reciprocal lattice* is spanned by the following reciprocal-lattice primitive vectors $\mathbf{b}_1$ and $\mathbf{b}_2$:

$$\mathbf{b}_1 = \frac{2\pi\mathbf{a}_2\times\mathbf{e}_3}{\mathbf{a}_1\cdot(\mathbf{a}_2\times\mathbf{e}_3)}, \quad \mathbf{b}_2 = \frac{2\pi\mathbf{e}_3\times\mathbf{a}_1}{\mathbf{a}_1\cdot(\mathbf{a}_2\times\mathbf{e}_3)}, \tag{2}$$

where $\mathbf{e}_3=(0,0,1)$ is a unit vector pointing vertically upward. Any vector $\mathbf{K}$ connecting two nodes in the reciprocal lattice can be represented by

$$\mathbf{K}(n_1,n_2) = n_1\mathbf{b}_1 + n_2\mathbf{b}_2, \tag{3}$$

where n_1 and n_2 are integers. Since $\mathbf{a}_i\cdot\mathbf{b}_j=2\pi\delta_{ij}$, the following identity holds:

$$e^{i\mathbf{K}(n_1,n_2)\cdot\mathbf{R}(m_1,m_2)} = 1, \tag{4}$$

for any integers $m_1,m_2;n_1,n_2$. For the special case of a rectangular lattice, $\mathbf{a}_1\cdot\mathbf{a}_2=0$. The primitive vectors of the reciprocal lattice are simply $\mathbf{b}_1=2\pi\mathbf{a}_1/|\mathbf{a}_1|^2$ and $\mathbf{b}_2=2\pi\mathbf{a}_2/|\mathbf{a}_2|^2$ which are also orthogonal to each other.

Let the incident wave number vector be $\mathbf{k}_1$. Another wave in the direction of $\mathbf{k}_j$ is said to be resonantly scattered if $\mathbf{k}_j$ and $\mathbf{k}_1$ are related to a reciprocal lattice vector $\mathbf{K}_{1,j}$ by the Bragg condition:

$$\mathbf{k}_j = \mathbf{k}_1 + \mathbf{K}_{1,j}, \tag{5}$$

where the double subscripts indicate the direction of the reciprocal lattice vector, i.e., $\mathbf{K}_{i,j}$ points from the tip of $\mathbf{k}_i$ to the tip of $\mathbf{k}_j$. If more than one wave is resonantly scattered, Eq. (3) implies that any two resonated wave vectors are related by

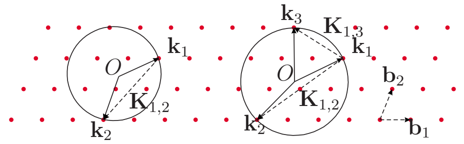

FIG. 1. (Color online) Demonstration of Bragg resonance wave vectors by Ewald construction: A two-wave Bragg resonance $N=2$ (left) and a three-wave Bragg resonance $N=3$ (right).

$$\mathbf{k}_j = \mathbf{k}_i + \mathbf{K}_{i,j}. \tag{6}$$

If the periodic array is infinite in extent, Bloch's theorem [3,4] requires that a linear wave solution obeys the condition

$$\phi[\mathbf{r} + \mathbf{R}(m_1,m_2)] = e^{i\mathbf{k}_j\cdot\mathbf{R}(m_1,m_2)}\phi(\mathbf{r}). \tag{7}$$

For a given lattice, the method of Ewald construction in crystallography facilitates the finding of the directions of the resonantly scattered waves $\mathbf{k}_j$, $j\neq 1$, from the reciprocal lattice and the incident wave number vector $\mathbf{k}_1$ [3,4]. Figure 1 shows a reciprocal lattice plane spanned by the primitive vectors $\mathbf{b}_1$ and $\mathbf{b}_2$. Let the tip of $\mathbf{k}_1$ coincide with a node. If another node P_2 falls on the circle centered at the tail O of $\mathbf{k}_1$, the vector $\overrightarrow{OP_2}$ is the resonantly scattered wave vector $\mathbf{k}_2$. Depending on the incident wave vector and the reciprocal lattice geometry, there can be N coupled vectors $\mathbf{k}_j$, $j=1,\ldots,N$ satisfying the Bragg resonance condition (5) [47]. Two examples of resonated wave vectors are shown in Fig. 1. A case of two-wave resonance is shown on the left, where $\mathbf{k}_2$ represents the scattered wave with $\mathbf{K}_{1,2}=\mathbf{k}_2-\mathbf{k}_1=-\mathbf{b}_1-2\mathbf{b}_2$. A three-wave resonance is shown on the right, where $\mathbf{k}_2$ and $\mathbf{k}_3$ are the scattered waves with $\mathbf{K}_{1,2}=\mathbf{k}_2-\mathbf{k}_1=-2\mathbf{b}_1-2\mathbf{b}_2$ and $\mathbf{K}_{1,3}=\mathbf{k}_3-\mathbf{k}_1=-2\mathbf{b}_1+\mathbf{b}_2$. For a shorter incident wave (larger $k=|\mathbf{k}_1|$), the total number of resonated waves can be greater.

For a given lattice and scattering configuration found by Ewald construction, we shall first derive the equations coupling the envelopes of the incident and $N-1$ resonantly scattered waves. Small detuning from perfect resonance is allowed.

III. LINEARIZED WATER-WAVE THEORY AND PERTURBATION PROBLEMS

Assuming irrotationality, the velocity potential must satisfy

$$\nabla^2\Phi + \frac{\partial^2\Phi}{\partial z^2} = 0, \quad -H\leqslant z\leqslant 0, \tag{8}$$

everywhere in water, where $\boldsymbol{\nabla}$ is the gradient operator in the horizontal plane (x,y). On the sea surface, the atmospheric pressure is assumed to be constant. The kinematic and dynamic conditions can be combined to give

$$\frac{\partial^2\Phi}{\partial t^2}+g\frac{\partial\Phi}{\partial z}=0, \quad z=0. \tag{9}$$

Let $(\mathbf{r}',z)$ be defined as the local cylindrical polar coordinate centered at the lattice node $\mathbf{R}(m_1,m_2)$, then the position of any point in space is

$$(\mathbf{r},z)=[\mathbf{R}(m_1,m_2)+\mathbf{r}',z]. \tag{10}$$

On the boundary of the cylinder, the normal flux must vanish,

$$\frac{\partial\Phi}{\partial r'}=0, \quad r'=|\mathbf{r}-\mathbf{R}(m_1,m_2)|=a, \quad \text{for all } m_1,m_2. \tag{11}$$

Finally, let the sea depth be constant. No vertical flux requires

$$\frac{\partial\Phi}{\partial z}=0, \quad z=-H. \tag{12}$$

It is well known that for vertical cylinders in water of constant depth, the mathematical problem is reducible to one for two-dimensional acoustic scattering. We now add the assumption that the cylinder radius a is much smaller than the typical wave length $2\pi/k$ so that

$$\mu=ka \ll 1 \tag{13}$$

is a small parameter. It is well known in acoustics since Rayleigh [38] that the scattered wave from one small cylinder is of the order $O(\mu^2)$ compared to the incident wave. It can also be shown that Bragg scattering by a large number of cylinders in a long channel is no longer weak if $N=O(\mu^{-2})$ [39,40]. This suggests the asymptotic method of multiple scales for describing the wave field almost everywhere except in the small neighborhood of the cylinders. For this *outer field* we introduce fast and slow variables

$$x,y,z,t; \quad X=\mu^2x, \quad Y=\mu^2y, \quad T=\mu^2t, \tag{14}$$

so that x,y,z,t describe the fast motion characterized by the length and time scales of $1/k, 1/\omega$, while X,Y,T describe the slow variation of the envelope. The outer potential is expanded as follows:

$$\Phi=[\phi_1+\mu^2\phi_2^{\text{out}}+O(\mu^4)]e^{-i\omega t}+\text{c.c.}, \tag{15}$$

where ϕ_1 and ϕ_2^{out} are functions of $(x,y,z;X,Y,T)$. Substituting Eq. (15) into the governing equations (8), (9), and (12), we obtain the perturbation equations for the outer potentials ϕ_1 and ϕ_2^{out}.

A. First order problem

At the first order, the outer velocity potential ϕ_1 is governed by the boundary value problem,

$$\nabla^2\phi_1+\frac{\partial^2\phi_1}{\partial z^2}=0, \quad -H\leqslant z\leqslant 0, \tag{16}$$

$$\frac{\partial\phi_1}{\partial z}-\frac{\omega^2}{g}\phi_1=0, \quad z=0, \tag{17}$$

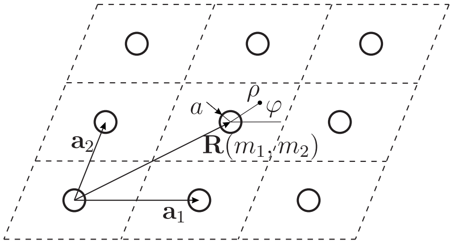

FIG. 2. Unit cell in a cylinder lattice constructed by $\mathbf{a}_1$ and $\mathbf{a}_2$. A typical local polar coordinate system is shown around $\mathbf{R}(m_1,m_2)$.

$$\frac{\partial\phi_1}{\partial z}=0, \quad z=-H. \tag{18}$$

In addition, we require that ϕ_1 must satisfy Bloch's theorem (7) on the short scale.

Because the local effect of scattering by the small cylinders is only of order $O(\mu^2)$, no boundary condition on the cylinder surfaces is needed for ϕ_1. The cylinders are mathematically absent at the first order.

The boundary-value problem for ϕ_1 is homogeneous and governs the fast variations in a unit cell, depicted in Fig. 2. The solution is formally the sum of all mutually resonant progressive waves,

$$\phi_1=\sum_{j=1}^{N}A_j(X,Y,T)\psi_j(x,y,z), \tag{19}$$

where

$$\psi_j(x,y,z)=Z(z)e^{i\mathbf{k}_j\cdot\mathbf{r}}, \tag{20}$$

with all $\mathbf{k}_j=k(\cos\beta_j\mathbf{i}+\sin\beta_j\mathbf{j})$ determined by Bragg condition (5). The potential amplitudes of the jth resonated wave A_j are yet unknown. $Z(z)$ is the vertical profile given by

$$Z(z)=-\frac{ig}{2\omega}\frac{\cosh k(z+H)}{\cosh kH}, \tag{21}$$

with the dispersion relation

$$\omega^2=gk\tanh kH. \tag{22}$$

B. Second-order problem at $O(\mu^2)$

Upon substituting Eq. (15) into Eqs. (8), (9), (12), and (7) collecting terms of μ^2, we obtain the boundary value problem for the second-order outer potential ϕ_2^{out}:

$$\nabla^2\phi_2^{\text{out}}+\frac{\partial^2\phi_2^{\text{out}}}{\partial z^2}=-2\bar{\boldsymbol{\nabla}}\cdot\boldsymbol{\nabla}\phi_1, \quad \text{in fluid}, \tag{23}$$

$$\frac{\partial\phi_2^{\text{out}}}{\partial z}-\frac{\omega^2}{g}\phi_2^{\text{out}}=\frac{2i\omega}{g}\frac{\partial\phi_1}{\partial T}, \quad \text{on } z=0, \tag{24}$$

$$\frac{\partial\phi_2^{\text{out}}}{\partial z}=0, \quad \text{on } z=-H, \tag{25}$$

$$\phi_2^{\text{out}}[\mathbf{r}+\mathbf{R}(m_1,m_2)] = e^{i\mathbf{k}_j\cdot\mathbf{R}(m_1,m_2)}\phi_2^{\text{out}}(\mathbf{r}), \quad j=1,\ldots,N \tag{26}$$

In Eq. (23), $\bar{\boldsymbol{\nabla}}$ denotes the gradient operator with respect to the slow variables X and Y. On the cylinder surface, we must now impose the no-flux boundary condition. Let $[\rho \equiv |\mathbf{r}'| = |\mathbf{r}-\mathbf{R}(m_1,m_2)|, \varphi]$ be the local polar coordinates. Using Eq. (19), we get the radial gradient of ϕ_1 in the local polar coordinate system centered at $\mathbf{R}(m_1,m_2)$

$$\begin{aligned}\frac{\partial\phi_1}{\partial\rho} &= \sum_{j=1}^{N} A_j Z(z)\frac{\partial e^{i\mathbf{k}_j\cdot\mathbf{r}}}{\partial\rho}\\ &= Z(z)\sum_{j=1}^{N} A_j e^{i\mathbf{k}_j\cdot\mathbf{R}(m_1,m_2)}\frac{\partial e^{ik\rho\cos(\beta_j-\varphi)}}{\partial\rho}\\ &= Z(z)\sum_{j=1}^{N} ikA_j e^{i\mathbf{k}_j\cdot\mathbf{R}(m_1,m_2)}\cos(\beta_j-\varphi)e^{ik\rho\cos(\beta_j-\varphi)}.\end{aligned} \tag{27}$$

For small $\mu = ka$, Eq. (27) on the cylinder surface $\rho = a$ can be approximated by

$$\left.\frac{\partial\phi_1}{\partial\rho}\right|_{\rho=a} = Z(z)\sum_{j=1}^{N} kA_j e^{i\mathbf{k}_j\cdot\mathbf{R}(m_1,m_2)}\left\{ i\cos(\varphi-\beta_j) - \frac{\mu}{2}[1+\cos 2(\varphi-\beta_j)]\right\} + O(\mu^2). \tag{28}$$

Such a finite gradient on the surface of a small cylinder can be canceled by a $O(\mu^2)$ potential only if the latter has a large local gradient. An inner correction is needed.

We now split the unit cell into two parts. In the *far field* defined by $k|\mathbf{r}'| = O(1)$, the outer potential $\mu^2\phi_2^{\text{out}}$ satisfies Eqs. (23)–(26), while its radial gradient is of negligible importance in the neighborhood of the cylinder.

In the *near field*, $\rho = |\mathbf{r}'| = O(a)$, an inner correction $\mu^2\phi_2^{\text{in}}$ must be added, which needs to satisfy only the homogeneous version of the governing equations (23)–(25), and to vanish at $\rho \gg a$. But its radial gradient must cancel $\partial\phi_1/\partial\rho$ given in Eq. (28), i.e.,

$$\frac{\partial\phi_2^{\text{in}}}{\partial\rho} = -Z(z)\sum_{j=1}^{N} kA_j e^{i\mathbf{k}_j\cdot\mathbf{R}_{m_1,m_2}}\left\{\frac{i\cos(\varphi-\beta_j)}{\mu^2} - \frac{1+\cos 2(\varphi-\beta_j)}{2\mu}\right\}, \quad \text{on } \rho = a. \tag{29}$$

Writing the inner correction potential as

$$\phi_2^{\text{in}} = Z(z)\chi(\rho,\varphi),$$

it is easy to show that χ satisfies the two-dimensional Laplace equation in the horizontal plane with an error of $O(\mu^2)$. The solution can be immediately found to be

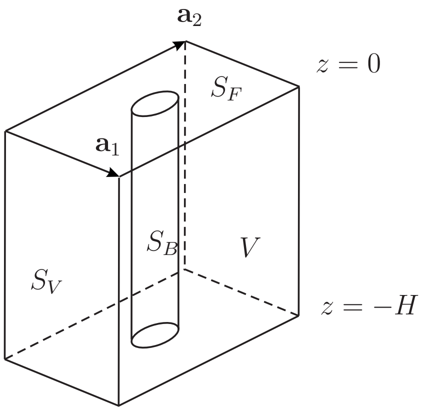

FIG. 3. A unit cell.

$$\phi_2^{\text{in}} = Z(z)\sum_{j=1}^{N} A_j e^{i\mathbf{k}_j\cdot\mathbf{R}(m_1,m_2)}\left\{\frac{\log k\rho}{2} + \frac{i}{\mu}\frac{a}{\rho}\cos(\varphi-\beta_j) - \frac{1}{4}\frac{a^2}{\rho^2}\cos 2(\varphi-\beta_j)\right\} + O(\mu^0). \tag{30}$$

For later use we record its value on the cylinder $\rho = a$:

$$\phi_2^{\text{in}} = Z(z)\sum_{j=1}^{N} A_j e^{i\mathbf{k}_j\cdot\mathbf{R}(m_1,m_2)}\left\{\frac{\log\mu}{2} + \frac{i}{\mu}\cos(\varphi-\beta_j) - \frac{1}{4}\cos 2(\varphi-\beta_j)\right\} + O(\mu^0). \tag{31}$$

Note that the entire second-order solution is

$$\phi_2 = \phi_2^{\text{out}} + \phi_2^{\text{in}}, \tag{32}$$

in which the outer field away from the cylinder is dominated by ϕ_2^{out} but the near field around the cylinder is dominated by ϕ_2^{in}. Their sum ϕ_2 is uniformly valid everywhere in the unit cell surrounding the cylinder as shown in Fig. 3. Instead of solving the entire inhomogeneous second-order problem explicitly, it suffices to examine its solvability in order to derive the envelope equations for A_j.

IV. ENVELOPE (COUPLED-MODE) EQUATIONS

A. Solvability of ϕ_2

Recall that every $\psi_j, j=1,\ldots,N$ defined in Eq. (20) satisfies the homogeneous version of the boundary value problem (23)–(26). Let us define a unit cell to be the fluid column of height H and of the base defined by the primitive vectors $\mathbf{a}_1$ and $\mathbf{a}_2$, as shown in Fig. 3. For each $j=1,\ldots,N$, we apply Green's identity to ψ_j^* and ϕ_2 over the unit cell, where ψ_j^* denotes the complex conjugate of ψ_j,

$$\int\int\int_V \left\{\phi_2\left(\nabla^2 + \frac{\partial^2}{\partial z^2}\right)\psi_j^* - \psi_j^*\left(\nabla^2 + \frac{\partial^2}{\partial z^2}\right)\phi_2\right\}dV = \int\int_{\partial V}\left(\phi_2\frac{\partial\psi_j^*}{\partial n} - \psi_j^*\frac{\partial\phi_2}{\partial n}\right)dS. \tag{33}$$

The bounding surface of V, denoted by ∂V, consists of the free surface S_F, the cylinder surface S_B, the vertical surfaces S_V and the sea bottom at $z=-H$. The above identity amounts to the solvability condition for the inhomogeneous problem of ϕ_2, and should lead to the evolution equations for A_j. We now evaluate the integrals.

Substituting Eqs. (32), (23), and (20) into the volume integral on the left side of Eq. (33) and noticing that ϕ_2^{in} satisfies the homogeneous Laplace equation in V, we obtain

$$\text{LHS}(33) = 2i\sum_{h=1}^{N} \mathbf{k}_h \cdot \bar{\boldsymbol{\nabla}} A_h \int_{-H}^{0} Z^2(z)dz \int\int_{S_F} e^{i(\mathbf{k}_h-\mathbf{k}_j)\cdot\mathbf{r}} dS. \tag{34}$$

Since the linear dimension of the unit cell is comparable to the incident wavelength, $k(|\mathbf{a}_1|,|\mathbf{a}_2|)=O(1)$. The cross-sectional area of a cylinder is much smaller than that of the unit cell: $\mathcal{A}_F=\mathcal{A}-\pi a^2=\mathcal{A}[1+O(\mu^2)]\approx\mathcal{A}$, where $\mathcal{A}_F$ is the area of the free surface S_F. The surface integral in Eq. (34) can be approximated by

$$\begin{aligned}\int\int_{S_F} e^{i(\mathbf{k}_h-\mathbf{k}_j)\cdot\mathbf{r}} dS &= \int\int_{\mathcal{A}} e^{i(\mathbf{k}_h-\mathbf{k}_j)\cdot\mathbf{r}} dS + O(\mu^2) \\ &= \delta_{jh}\mathcal{A} + O(\mu^2).\end{aligned} \tag{35}$$

The last identity is proven in Appendix A [see Eq. (A6)].

Substituting Eq. (35) into Eq. (34) and dropping terms of order $O(\mu^2)$, we get

$$\begin{aligned}\text{LHS}(33) &= 2i\mathcal{A}\int_{-H}^{0} Z^2(z)dz \sum_{h=1}^{N} \mathbf{k}_h \cdot \bar{\boldsymbol{\nabla}} A_h \delta_{jh} \\ &= 2i\mathcal{A}\int_{-H}^{0} dz\, Z^2(z)(\mathbf{k}_j \cdot \bar{\boldsymbol{\nabla}} A_j).\end{aligned} \tag{36}$$

In the surface integral on the right-hand side of Eq. (33), there is no contribution from the sea bottom. Contribution from the outer vertical boundaries S_V of the unit cell also vanishes by Bloch's condition for ϕ_2^{out} and the rapid vanishing of ϕ_2^{in} away from the cylinder. Making use of the free surface conditions (24) for ϕ_2^{out}, Eq. (20) for ψ_j^* and the homogeneous free surface condition for ϕ_2^{in}, the integral over the free surface S_F on the right side of Eq. (33) becomes

$$\begin{aligned}\int\int_{S_F}\left(\phi_2\frac{\partial\psi_j^*}{\partial z} - \psi_j^*\frac{\partial\phi_2}{\partial z}\right)dS &= -\frac{2i\omega}{g}\int\int_{S_F}\psi_j^*\frac{\partial\phi_1}{\partial T}dS \\ &= -\frac{2i\omega}{g}Z^2(0)\sum_{h=1}^{N}\frac{\partial A_h}{\partial T}\int\int_{S_F} e^{i(\mathbf{k}_h-\mathbf{k}_j)\cdot\mathbf{r}}dS \\ &= -\frac{2i\omega\mathcal{A}}{g}Z^2(0)\frac{\partial A_j}{\partial T},\end{aligned} \tag{37}$$

where terms of $O(\mu^2)$ have been dropped.

The surface integral in Eq. (33) over the cylinder is evaluated in Appendix B, with the result

$$I_B = \sum_{h=1}^{N} \pi A_h[1-2\cos(\beta_j-\beta_h)]\int_{-H}^{0} Z^2(z)dz + O(\mu). \tag{38}$$

Note that I_B is of order $O(\mu^0)$ and is independent of the cylinder radius a.

With these results Eq. (33) reduces to

$$\begin{aligned}&\frac{\partial A_j}{\partial T} + \frac{gk}{\omega}\int_{-H}^{0}\frac{Z^2(z)}{Z^2(0)}dz\left(\frac{\mathbf{k}_j}{k}\cdot\bar{\boldsymbol{\nabla}}\right)A_j \\ &\quad = -\frac{i}{2}\frac{\pi}{k\mathcal{A}}\frac{gk}{\omega}\int_{-H}^{0}\frac{Z^2(z)}{Z^2(0)}dz\sum_{h=1}^{N}[1-2\cos(\beta_j-\beta_h)]A_h.\end{aligned} \tag{39}$$

The z integral in Eq. (39) is just the group speed in open water,

$$\begin{aligned}\frac{gk}{\omega}\int_{-H}^{0}\frac{Z^2(z)}{Z^2(0)}dz &= \frac{gk}{\omega}\int_{-H}^{0}\frac{\cosh^2 k(z+H)}{\cosh^2 kH}dz \\ &= \frac{\omega}{2k}\left(1+\frac{2kH}{\sinh 2kH}\right) \equiv C_g.\end{aligned} \tag{40}$$

Let

$$\Omega_0 = \frac{\pi C_g}{k\mathcal{A}}, \tag{41}$$

which has the dimension of frequency, and

$$\mathbf{C}_g^{(j)} = C_g\frac{\mathbf{k}_j}{k}, \quad j=1,\ldots,N, \tag{42}$$

the wave envelope equations (39) reduce to a more concise form:

$$\begin{aligned}&\frac{\partial A_j}{\partial T} + \mathbf{C}_g^{(j)}\cdot\bar{\boldsymbol{\nabla}} A_j \\ &\quad = -\frac{1}{2}i\Omega_0\sum_{h=1}^{N}[1-2\cos(\beta_j-\beta_h)]A_h, \quad j=1,\ldots,N.\end{aligned} \tag{43}$$

Returning to natural coordinates via $X=k^2a^2x$, $Y=k^2a^2y$, and $T=k^2a^2t$, the envelope equations read

$$\begin{aligned}&\frac{\partial A_j}{\partial t} + \mathbf{C}_g^{(j)}\cdot\boldsymbol{\nabla} A_j \\ &\quad = -\frac{i(ka)^2\Omega_0}{2}\sum_{h=1}^{N}[1-2\cos(\beta_j-\beta_h)]A_h, \quad j=1,\ldots,N.\end{aligned} \tag{44}$$

The coupling coefficient $(ka)^2\Omega_0=kC_g(\pi a^2/\mathcal{A})$ on the right side of Eq. (44) is proportional to volume density of the cylinders in water. Recall that N and k_j hence β_j are determined by Bragg condition (5). The system of equations (43) or (44) is the two-dimensional extension of the one-dimensional *coupled-mode equations* in optics [5] and in other fields. In open water without cylinders, Eq. (43) reduce to

$$\frac{\partial A_j}{\partial T} + \mathbf{C}_g^{(j)} \cdot \bar{\boldsymbol{\nabla}} A_j = 0, \quad j = 1, \ldots, N, \tag{45}$$

which is the well-known law of wave-action conservation (see, e.g., [41]).

Several immediate consequences can be deduced.

B. Energy conservation

Let us multiply both sides of Eq. (43) by A_j^* and adding the resulting equation with its complex conjugate. After summation over j, we obtain

$$\sum_{j=1}^{N} \left(\frac{\partial |A_j|^2}{\partial T} + \mathbf{C}_g^{(j)} \cdot \bar{\boldsymbol{\nabla}} |A_j|^2 \right) = -\frac{\Omega_0}{2} \sum_{j=1}^{N} \sum_{h=1}^{N} [1 - 2\cos(\beta_j - \beta_h)] \times (iA_h A_j^* - iA_h^* A_j). \tag{46}$$

By changing the second term in the last parentheses on the right from $A_h^* A_j$ to $A_j^* A_h$, the double series is unaltered, hence must be zero, yielding

$$\frac{\partial}{\partial T} \sum_{j=1}^{N} |A_j|^2 + \sum_{j=1}^{N} (\mathbf{C}_g^{(j)} \cdot \bar{\boldsymbol{\nabla}} |A_j|^2) = 0. \tag{47}$$

Thus the total energy is conserved in the cylinder array. This result can be used to check the correctness of algebra later.

C. Limiting case 1: No Bragg resonance

If no scattered wave is resonated in the cylinder array by the incident wave, then $N=1$. The envelope of the incident wave satisfies

$$\frac{\partial A_1}{\partial T} + \mathbf{C}_g^{(1)} \cdot \bar{\boldsymbol{\nabla}} A_1 = \frac{1}{2} i\Omega_0 A_1. \tag{48}$$

which has the solution

$$A_1(X,Y,T) = A_1(X\cos\beta_1 + Y\sin\beta_1 - C_g T)e^{i\Omega_0 T/2}, \tag{49}$$

Using Eq. (49), the corresponding free surface elevation is

$$\zeta = \frac{1}{2} A_1 e^{i(\mathbf{k}_1 \cdot \mathbf{r} - \omega t)} + \text{c.c.} = \frac{1}{2} A_1 (X\cos\beta_1 + Y\sin\beta_1 - C_g T) e^{i\mathbf{k}_1 \cdot \mathbf{r}} e^{-i(\omega - \mu^2 \Omega_0/2)t}. \tag{50}$$

Thus the leading-order effect of the cylinder array is to introduce a small frequency downshift $\mu^2\Omega_0/2$ in the incident wave. The wave envelope advances at the group velocity, without changing its profile. The small scattered wave can in principle be obtained at the next order, not pursued here.

D. Limiting case 2: A linear array in a long channel

A linear array along the centerline of a long and straight channel is equivalent to one period of a rectangular array when the incident wave is directed along one set of parallel rows. The primitive lattice vectors $\mathbf{a}_1 = a_1\mathbf{i}$ and $\mathbf{a}_2 = a_2\mathbf{j}$ of the lattice are orthogonal to each other. The reciprocal lattice is then constructed by the primitive vectors $\mathbf{b}_1 = 2\pi\mathbf{i}/a_1$ and $\mathbf{b}_2 = 2\pi\mathbf{j}/a_2$ following (2), so that a reciprocal lattice vector is expressed by

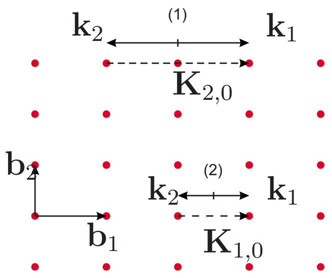

FIG. 4. (Color online) Bragg resonance by normally incident waves. The reciprocal lattice spanned by $\mathbf{b}_1$ and $\mathbf{b}_2$. Case (1): Bragg resonance with $\mathbf{k}_1 = -\mathbf{k}_2 = \mathbf{b}_1/2$, $n_1 = 2$; case (2): Bragg resonance with $\mathbf{k}_1 = -\mathbf{k}_2 = \mathbf{b}_1$, $n_1 = 1$.

$$\mathbf{K}_{n_1,n_2} = n_1\mathbf{b}_1 + n_2\mathbf{b}_2 = \frac{2\pi n_1}{a_1}\mathbf{i} + \frac{2\pi n_2}{a_2}\mathbf{j}. \tag{51}$$

Assume further that the incident wave train arrives from $x \sim -\infty$ along the x direction which is parallel to $\mathbf{a}_1$, i.e., $\mathbf{k}_1 = k\mathbf{i}$. The reflected wave with $\mathbf{k}_2 = -k\mathbf{i}$ can be resonated and satisfies the Bragg condition (5):

$$\mathbf{k}_1 - \mathbf{k}_2 = 2k\mathbf{i} = \mathbf{K}_{n,0} = \frac{2\pi n}{a_1}\mathbf{i}, \tag{52}$$

where $n_1 = n$ is any positive integer and $n_2 = 0$. Wave propagation is one-dimensional and is equivalent to Bragg scattering by a linear array along the centerline of a long channel of width a_2. Two examples of one-dimensional resonance satisfying Eq. (52) are shown in Fig. 4.

By substituting $k = n\pi/a_1$, $\beta_1 = 0$, and $\beta_2 = \pi$ into Eq. (43), we obtain the following pair of couple-mode equations for the incident (A_1) and reflected (A_2) envelopes:

$$\frac{\partial A_1}{\partial T} + C_g \frac{\partial A_1}{\partial X} = -\frac{1}{2} i\Omega_0(-A_1 + 3A_2), \tag{53a}$$

$$\frac{\partial A_2}{\partial T} - C_g \frac{\partial A_2}{\partial X} = -\frac{1}{2} i\Omega_0(3A_1 - A_2), \tag{53b}$$

where

$$\Omega_0 = \frac{\pi C_g}{k\mathcal{A}} = \frac{\pi C_g}{\frac{n\pi}{a_1} a_1 a_2} = \frac{C_g}{n a_2}. \tag{54}$$

These results have been derived independently for waves in a long channel of width a_2 with a linear array of cylinders along the center line [39,40], and can be combined to yield a single equation, which resembles the Klein-Gordon equation, for A_1 (or A_2).

V. TWO-DIMENSIONAL SCATTERING BY A WIDE STRIP OF CYLINDERS

In principle the system (43) can be used to study resonant diffraction by a large area of cylinders of any plan form. For explicit analysis, we apply it to a long and straight strip of cylinder array, which may idealize the supporting structure of an offshore airport. Let the width L' of the strip be of order $O(1/k\mu^2)$ in the x- (east-west) direction and the length be infinite in $\pm y$ (north-south) directions. A train of plane incident waves arrives from the south-west at an angle β_1 with respect to the x-axis.

Let the superscripts $-$ and $+$ be used to distinguish the open-water regions to the west and to the east of the strip respectively, and let symbols without a superscript denote quantities inside the strip. The wave potentials in the three zones are

$$\Phi_1 = Z(z)\sum_{j=1}^{N} A_j(X,Y,T),$$

$$\text{where } A_j = \begin{cases} A_j^-, & X<0 \\ A_j, & 0 \leqslant X \leqslant L \\ A_j^+, & X>L, \end{cases} \qquad (55)$$

with $L=\mu^2 L'$.

We allow a slight detuning of the incident wave,

$$A_1^-(X,Y,T) = A_0 e^{i(\mathcal{K}\cos\beta_1 X + \mathcal{K}\sin\beta_1 Y - \Omega T)}, \quad X<0. \qquad (56)$$

where $\mu^2\mathcal{K}$ is the detuning wave number and $\mu^2\Omega$ the detuning frequency, related by $\mathcal{K}=\Omega/C_g$. For simplicity the vector $\mathcal{K}(\cos\beta_1, \sin\beta_1)$ is assumed to be parallel to $\mathbf{k}_1$.

In the cylinder region $0 \leqslant X \leqslant L$, the governing equations for the Bragg-resonated envelopes are Eq. (43). In general $M(\leqslant N)$ waves propagate forward to the east ($\cos\beta_j>0$) and the remaining $N-M$ waves propagate backward to the west ($\cos\beta_j<0$). Requiring continuity of the dynamic pressure $p=-\rho_0\partial\Phi_1/\partial t$ (ρ_0 is the water density) and the normal velocity $\partial\Phi_1/\partial x$ along the edges $X=0,L$, it can be shown that the amplitudes of waves in the same directions must be continuous (see Appendix in [36]). Specifically, along the left edge $X=0$, the envelopes of the incident and all backward-scattered waves are continuous,

$$A_1^-(0,Y,T) = A_1(0,Y,T), \qquad (57)$$

and

$$A_j^-(0,Y,T) = A_j(0,Y,T), \quad \text{if } \cos\beta_j<0, \qquad (58)$$

but all forward waves except the incident wave must vanish

$$A_j(0,Y,T) = 0, \quad \text{if } \cos\beta_j>0; \quad j \neq 1. \qquad (59)$$

Similarly, along the right edge $X=L$, all forward waves are continuous

$$A_j^+(L,Y,T) = A_j(L,Y,T), \quad \text{if } \cos\beta_j>0, \qquad (60)$$

while all backward waves must vanish,

$$A_j(L,Y,T) = 0, \quad \text{if } \cos\beta_j<0. \qquad (61)$$

Together these matching conditions provide N boundary conditions for the wave envelopes $A_j(X,Y,T)$, $j=1,\ldots,N$. The boundary-value problems for all A_j can be solved.

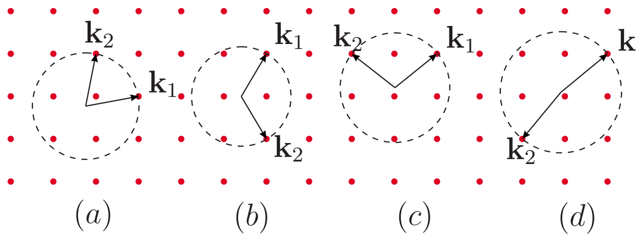

(a) (b) (c) (d)

FIG. 5. (Color online) Four scattering configurations in the reciprocal lattice. The incident wave vector $\mathbf{k}_1=k(\cos\beta_1,\sin\beta_1)$ always points to the northeast. The scattered wave vector is $\mathbf{k}_2=k(\cos\beta_2,\sin\beta_2)$. (a) Forward scattering to the northeast: $0\leqslant\beta_2<\pi/2$; (b) forward scattering to the southeast: $-\pi/2<\beta_2<0$; (c) backward scattering (reflection) to the northwest: $\pi/2<\beta_2\leqslant\pi$; (d) backward scattering (reflection) to the southwest: $-\pi<\beta_2<-\pi/2$.

We now discuss the explicit solutions for two simple cases: (i) One scattered wave ($N=2$) and (ii) two scattered waves ($N=3$).

VI. ONE SCATTERED WAVE: $N=2$

Without loss of generality we limit the direction of the incident wave to $0<\beta_1<\pi/2$, i.e., pointing to the northeast. By Ewald construction, one finds four possibilities for the scattered waves, for four different magnitudes of k. Two are scattered forward: $0\leqslant\beta_2<\pi/2$ [Fig. 5(a), forward-positive] and $-\pi/2<\beta_2<0$ [Fig. 5(b), forward-negative]. Two are scattered backward (reflection): $\pi/2<\beta_2\leqslant\pi$ [Fig. 5(c), backward-positive], and $-\pi<\beta_2<-\pi/2$ [Fig. 5(d), backward-negative]. Similar possibilities are known in x-ray diffraction by crystals [2].

A. Boundary-value problems for wave envelopes

With $N=2$, the governing equations for the wave envelopes A_j, $j=1,2$ in the strip $0\leqslant X\leqslant L$ and the envelopes $A_j^{\pm}$, $j=1,2$ outside the strip are given by Eqs. (43) and (45), respectively. By assuming

$$\begin{bmatrix} A_j^- \\ A_j \\ A_j^+ \end{bmatrix} = A_0 \begin{bmatrix} B_j^-(X) \\ B_j(X) \\ B_j^+(X) \end{bmatrix} e^{i(\mathcal{K}\sin\beta_1 Y - \Omega T)}, \quad j=1,2, \qquad (62)$$

we get

$$\frac{dB_1^-}{dX} = i\mathcal{K}\cos\beta_1 B_1^-, \qquad (63a)$$

$$\frac{dB_2^-}{dX} = \frac{i\mathcal{K}(1-\sin\beta_1\sin\beta_2)}{\cos\beta_2} B_2^-, \qquad (63b)$$

in the open water to the left ($X<0$),

$$\frac{dB_1}{dX} = \frac{i\Omega_0}{C_g}\left\{\left[\frac{1}{2\cos\beta_1} + \frac{\Omega}{\Omega_0}\cos\beta_1\right]B_1 + \frac{2\cos(\beta_1-\beta_2)-1}{2\cos\beta_1}B_2\right\}, \tag{64a}$$

$$\frac{dB_2}{dX} = \frac{i\Omega_0}{C_g}\left\{\frac{2\cos(\beta_1-\beta_2)-1}{2\cos\beta_2}B_1 + \left[\frac{1}{2\cos\beta_2} + \left(\frac{\Omega}{\Omega_0}\right)\frac{1-\sin\beta_1\sin\beta_2}{\cos\beta_2}\right]B_2\right\}, \tag{64b}$$

inside the strip $0 \leqslant X \leqslant L$, and

$$\frac{dB_1^+}{dX} = i\mathcal{K}\cos\beta_1 B_1^+, \tag{65a}$$

$$\frac{dB_2^+}{dX} = \frac{i\mathcal{K}(1-\sin\beta_1\sin\beta_2)}{\cos\beta_2}B_2^+, \tag{65b}$$

in the open water to the right ($X > L$). Use is made of the relation $\Omega = C_g\mathcal{K}$.

The solutions in open waters can be determined easily from the uncoupled equations. Inside the strip of cylinders, we write the coupled equations (64a) and (64b) in matrix form:

$$\frac{d}{dX}\begin{bmatrix} B_1 \\ B_2 \end{bmatrix} = \frac{i\Omega_0}{C_g}\mathbf{M}\begin{bmatrix} B_1 \\ B_2 \end{bmatrix}, \tag{66}$$

where $\mathbf{M}$ is the matrix

$$\mathbf{M} = \begin{bmatrix} M_{11} & M_{12} \\ M_{21} & M_{22} \end{bmatrix} \tag{67}$$

with the elements

$$M_{11} = \frac{1}{2\cos\beta_1} + \left(\frac{\Omega}{\Omega_0}\right)\cos\beta_1, \tag{68a}$$

$$M_{12} = \frac{2\cos(\beta_1-\beta_2)-1}{2\cos\beta_1}, \tag{68b}$$

$$M_{21} = \frac{2\cos(\beta_1-\beta_2)-1}{2\cos\beta_2}, \tag{68c}$$

$$M_{22} = \frac{1}{2\cos\beta_2} + \left(\frac{\Omega}{\Omega_0}\right)\frac{1-\sin\beta_1\sin\beta_2}{\cos\beta_2}. \tag{68d}$$

The matrix $\mathbf{M}$ hence the homogeneous second-order system (66) has the following characteristic equation:

$$\lambda^2 - (M_{11}+M_{22})\lambda + (M_{11}M_{22} - M_{12}M_{21}) = 0, \tag{69}$$

whose eigenvalues are

$$\lambda_{1,2} = \frac{(M_{11}+M_{22}) \pm \Delta^{1/2}}{2}, \tag{70}$$

where Δ is the discriminant

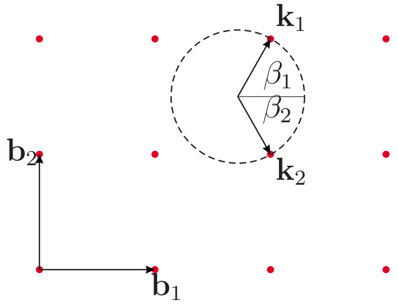

FIG. 6. (Color online) Forward-negative scattering by a square lattice of spacing a_1. The reciprocal space is spanned by $\mathbf{b}_1 = 2\pi\mathbf{i}/a_1$, and $\mathbf{b}_2 = 2\pi\mathbf{j}/a_1$. $\mathbf{k}_1$ and $\mathbf{k}_2$ are the incident and forward scattered wave vectors with wave number $k = 2\pi/\sqrt{3}a_1$, incident angle $\beta_1 = \pi/3$, and scattered wave angle $\beta_2 = -\pi/3$.

$$\begin{aligned}\Delta &= (M_{11}+M_{22})^2 - 4(M_{11}M_{22} - M_{12}M_{21}) \\ &= (M_{11}-M_{22})^2 + 4M_{12}M_{21} \\ &= \left[\frac{1}{2}\left(\frac{1}{\cos\beta_1} - \frac{1}{\cos\beta_2}\right) + \left(\frac{\Omega}{\Omega_0}\right)\frac{\cos(\beta_1-\beta_2)-1}{\cos\beta_2}\right]^2 \\ &\quad + \frac{[2\cos(\beta_1-\beta_2)-1]^2}{\cos\beta_1\cos\beta_2}.\end{aligned} \tag{71}$$

The solutions of $B_1(X)$ and $B_2(X)$ are linear combinations of $\exp(i\lambda_1\Omega_0 X/C_g)$ and $\exp(i\lambda_2\Omega_0 X/C_g)$. The coefficients are to be determined by the boundary conditions at $X = 0, L$. If $\Delta \geqslant 0$, both roots are real. There is no spatial attenuation or amplification along X in envelope amplitudes. Negative Δ corresponds to complex roots and the imaginary parts lead to amplitude attenuation or amplification. For a given cylinder array, the direction β_2 of the scattered wave for a given incident wave with wave number k and direction β_1 is first determined by Ewald's method. The discriminant Δ and the eigenvalues then depend on the detuning frequency Ω/Ω_0 as given by Eqs. (70) and (71). In the following, we discuss the effects of detuning frequency for different scattering configurations.

B. Forward scattering: $\cos\beta_2 > 0$

Assuming forward scattering, as illustrated by the reciprocal lattices shown in Fig. 6 and Fig. 10, we must have

$$B_1^-(X) = e^{i\mathcal{K}\cos\beta_1 X}, \quad B_2^-(X) = 0; \quad X < 0 \tag{72}$$

on the incidence side of the strip. With $\cos\beta_2 > 0$, the discriminant (71) can only be positive. Both eigenvalues are real. Inside the strip $0 \leqslant X \leqslant L$, the second-order differential system for $B_1(X)$ and $B_2(X)$ must satisfy two initial conditions at $X=0$: $B_1(0) = B_1^-(0) = 1$ and $B_2(0) = 0$. With these we find

$$B_1(X) = \frac{M_{11}-\lambda_2}{\lambda_1-\lambda_2}\exp\left[\frac{i\lambda_1\Omega_0 X}{C_g}\right] - \frac{M_{11}-\lambda_1}{\lambda_1-\lambda_2}\exp\left[\frac{i\lambda_2\Omega_0 X}{C_g}\right], \tag{73a}$$

$$B_2(X) = \frac{(M_{11}-\lambda_1)(M_{11}-\lambda_2)}{M_{12}(\lambda_1-\lambda_2)} \times \left\{ -\exp\left[\frac{i\lambda_1\Omega_0 X}{C_g}\right] + \exp\left[\frac{i\lambda_2\Omega_0 X}{C_g}\right]\right\}. \tag{73b}$$

The energy intensity of the transmitted wave is

$$|B_1(X)|^2 = \frac{(M_{11}-\lambda_1)^2 + (M_{11}-\lambda_2)^2}{(\lambda_1-\lambda_2)^2} - \frac{2(M_{11}-\lambda_1)(M_{11}-\lambda_2)}{(\lambda_1-\lambda_2)^2}\cos\left[\frac{(\lambda_1-\lambda_2)\Omega_0 X}{C_g}\right] = 1 - \frac{(2\cos(\beta_1-\beta_2)-1)^2}{2\Delta\cos\beta_1\cos\beta_2}\left(1-\cos\left[\frac{\Delta^{1/2}\Omega_0 X}{C_g}\right]\right), \tag{74}$$

Use has been made of Eq. (70), $(M_{11}-M_{22})^2 = \Delta - 4M_{12}M_{21}$ from Eq. (71), and $\lambda_1 - \lambda_2 = \Delta^{1/2}$. The forward-scattered wave intensity at X is

$$|B_2(X)|^2 = \frac{[(M_{11}-M_{22})^2-\Delta]^2}{8M_{12}^2\Delta}\left(1-\cos\left[\frac{\Delta^{1/2}\Omega_0 X}{C_g}\right]\right) = \frac{(2\cos(\beta_1-\beta_2)-1)^2}{2\Delta\cos^2\beta_2}\left(1-\cos\left[\frac{\Delta^{1/2}\Omega_0 X}{C_g}\right]\right). \tag{75}$$

These two results have been confirmed by the law of energy conservation (47), which can be integrated to give

$$\cos\beta_1|B_1(0)|^2 + \cos\beta_2|B_2(0)|^2 = \cos\beta_1|B_1(X)|^2 + \cos\beta_2|B_2(X)|^2. \tag{76}$$

The energy intensities of the transmitted wave $|B_1(X)|^2$ in Eq. (74) and the forward-scattered wave $|B_2(X)|^2$ in Eq. (75) are both oscillatory in X; the amplitude and period depend on the magnitude of the discriminant Δ, which depends on the detuning parameter Ω/Ω_0 according to Eq. (71).

We now present the numerical results for a square lattice of spacing a_1. The reciprocal lattice geometry is shown in Fig. 6. In accordance with Ewald method we choose the incident wave number to be $k = 2\pi/\sqrt{3}a_1$ and the inclination $\beta_1 = \pi/3$. The scattered wave is inclined at the angle $\beta_2 = -\pi/3$. The two real eigenvalues λ_1 and λ_2 computed from Eq. (70) for a range of the detuning parameter Ω/Ω_0 are displayed in Fig. 7. The wave intensities $|B_1(X)|^2$ and $|B_2(X)|^2$ are of course oscillatory in X, as shown in Figs. 8(a) and 8(b), respectively. As the detuning parameter Ω/Ω_0 increases, the scattered wave becomes weaker due to the increase of Δ in the denominator. Spatial oscillations of $|B_1(X)|^2$ and $|B_2(X)|^2$ become more intense with the eigenvalue difference $\lambda_1 - \lambda_2 = \Delta^{1/2}$ which increase with the detuning, as shown in Fig. 7. Since no boundary condition is imposed at $X = L$, the strip width L does not affect the period and magnitude of the wave intensities $|B_1(X)|^2$ and $|B_2(X)|^2$. In other words, the solution holds for any finite width L.

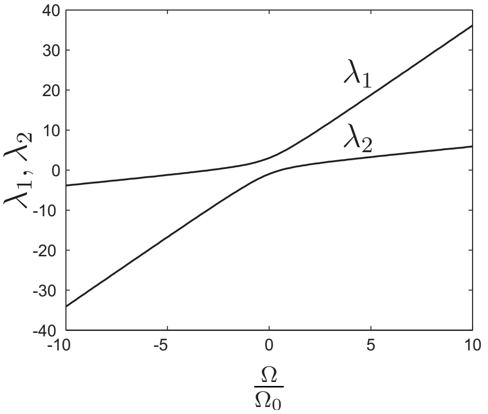

FIG. 7. Real eigenvalues λ_1 and λ_2 for the Bragg resonance in Fig. 6.

To examine the effect of detuning on the scattered wave intensity at the exit edge for some chosen width L, we get from Eq. (75)

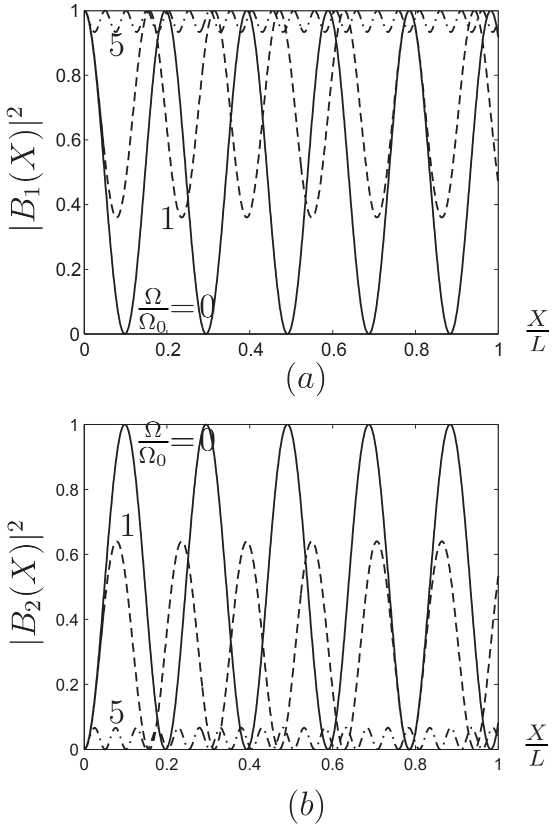

FIG. 8. (a) Transmitted wave intensity $|B_1(X)|^2$ and (b) the scattered wave intensity $|B_2(X)|^2$ over the cylinder strip with $\Omega_0 L/C_g = 8$. The number next to a curve gives the detuning parameter $\Omega/\Omega_0 = 0, 1, 5$.

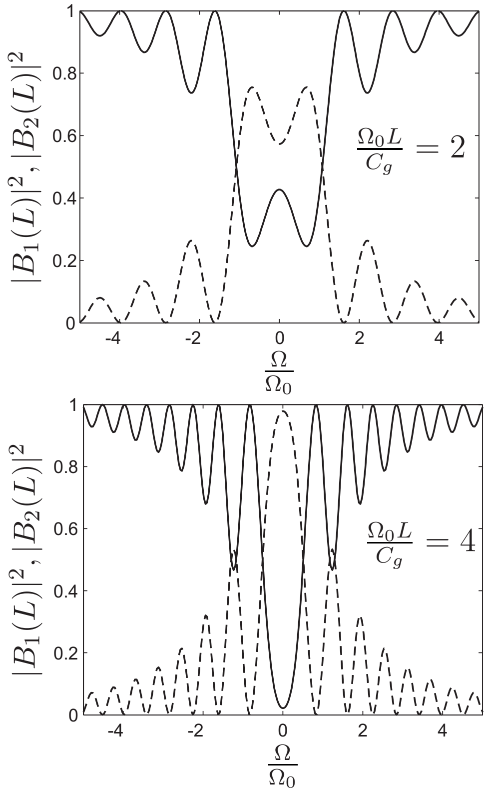

FIG. 9. Dependence of transmitted wave intensity $|B_1(L)|^2$ (solid curve) and forward scattered wave intensity $|B_2(L)|^2$ (dashed curve) on the detuning Ω/Ω_0 for strip width $\Omega_0 L/C_g=2$ and $\Omega_0 L/C_g=4$. The two resonated wave vectors are shown in Fig. 6: $\beta_1=\pi/3$ and $\beta_2=-\pi/3$.

$$|B_2(L)|^2=\frac{[2\cos(\beta_1-\beta_2)-1]^2}{2\Delta\cos^2\beta_2}\left(1-\cos\left[\frac{\Delta^{1/2}\Omega_0 L}{C_g}\right]\right). \tag{77}$$

The transmitted wave intensity is found from energy conservation (76):

$$|B_1(L)|^2=1-\frac{\cos\beta_2}{\cos\beta_1}|B_2(L)|^2 \tag{78}$$

after using $B(0)=1$ and $B_2(0)=0$. The dependence of $|B_1(L)|^2$ and $|B_2(L)|^2$ on the detuning frequency Ω/Ω_0 is plotted for two strip widths $\Omega_0 L/C_g=2$ and 4 in Fig. 9. It is evident that significant scattering takes place when tuning is perfect ($\Omega=0$). It can also be seen from Eq. (77) and Fig. 9 that for certain special values of the strip width

$$L=2\ell\pi\frac{C_g}{\Delta^{1/2}\Omega_0}, \quad \ell=0,1,\ldots, \tag{79}$$

there is no scattering but perfect transmission, i.e., $|B_2(L)|^2=0$ and $|B_1(L)|^2=1$. On the other hand, when the strip width is

$$L=(2\ell+1)\pi\frac{C_g}{\Delta^{1/2}\Omega_0}, \quad \ell=0,1,\ldots, \tag{80}$$

scattering at the exit edge $X=L$ is the greatest. The maximum scattered wave intensity is

$$|B_2(L)|^2_{\max}=\frac{[2\cos(\beta_1-\beta_2)-1]^2}{\Delta\cos^2\beta_2}. \tag{81}$$

The maximum $|B_2(L)|^2$ and the corresponding strip width L increase with decreasing Δ which depends on the detuning frequency Ω/Ω_0. When

$$\frac{\Omega}{\Omega_0}=\frac{\cos\beta_2/\cos\beta_1-1}{2[1-\cos(\beta_1-\beta_2)]}, \tag{82}$$

the first square bracket in Eq. (71) vanishes so that Δ reaches its minimum

$$\Delta_{\min}=\frac{[2\cos(\beta_1-\beta_2)-1]^2}{\cos\beta_1\cos\beta_2}. \tag{83}$$

Substituting Eq. (83) into Eq. (81), we get the maximum forward-scattered wave intensity

$$|B_2(L)|^2_{\max}=\frac{[2\cos(\beta_1-\beta_2)-1]^2}{\Delta_{\min}\cos^2\beta_2}=\frac{\cos\beta_1}{\cos\beta_2}. \tag{84}$$

The corresponding strip width must be

$$\begin{aligned}L&=(2\ell+1)\pi\frac{C_g}{\Delta_{\min}^{1/2}\Omega_0}\\&=\frac{(2\ell+1)\pi C_g}{\Omega_0}\frac{\sqrt{\cos\beta_1\cos\beta_2}}{|2\cos(\beta_1-\beta_2)-1|}, \quad \ell=0,1,\ldots\ .\end{aligned} \tag{85}$$

At these special values, $|B_1(L)|^2=0$. Thus while the incident wave enters the cylinder array in the direction $\beta_1=\pi/3$, only the scattered wave exits at $X=L$ in the direction $\beta_2=-\pi/3$. The cylinder strip acts as a virtual interface separating two media and causes an apparent negative refraction. This phenomenon is reminiscent of, but different from, the *negative refraction* occurring inside a medium with negative refractive index [42].

To the right of the strip $X>L$, we obtain by solving Eqs. (65a) and (65b) with the matching boundary conditions (60) at $X=L$ that

$$B_1^+(X)=B_1(L)e^{i\mathcal{K}\cos\beta_1(X-L)},$$

$$B_2^+(X)=B_2(L)e^{i\mathcal{K}_2(X-L)}, \quad X>L, \tag{86}$$

where

$$\mathcal{K}_2=\mathcal{K}\frac{1-\sin\beta_1\sin\beta_2}{\cos\beta_2}. \tag{87}$$

$B_1(L)$, $B_2(L)$ are obtained from Eqs. (73a) and (73b) as discussed above. The direction of the scattered wave envelope A_2^+ is

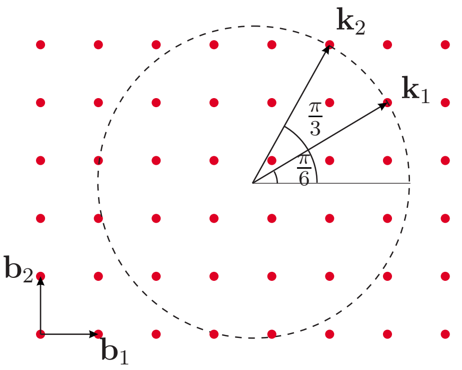

FIG. 10. (Color online) Forward-positive Bragg scattering in a square lattice of spacing a_1. The reciprocal vectors are $\mathbf{b}_1=2\pi\mathbf{i}/a_1$ and $\mathbf{b}_2=2\pi\mathbf{j}/a_1$. $\mathbf{k}_1$ and $\mathbf{k}_2$ are the incident and forward scattered wave vectors with $k=2(\sqrt{3}+1)\pi/a_1$, $\beta_1=\pi/6$, and $\beta_2=\pi/3$.

$$\varphi_2=\tan^{-1}\left(\frac{\sin\beta_1\cos\beta_2}{1-\sin\beta_1\sin\beta_2}\right)=\tan^{-1}\left(\frac{\sin\beta_1}{\cos\beta_1}\frac{\cos\beta_1\cos\beta_2}{1-\sin\beta_1\sin\beta_2}\right). \quad (88)$$

Since $\cos(\beta_1-\beta_j)\leqslant 1$, it follows by simple trigonometry that

$$\frac{\cos\beta_1\cos\beta_2}{1-\sin\beta_1\sin\beta_2}\leqslant 1. \quad (89)$$

Equation (88) implies $0<\varphi_2\leqslant\beta_1$. Thus, although the scattered wave is directed forward to the south-east $(-\pi/2<\beta_2<0)$, its envelope (hence energy) is directed to the northeast at an angle no greater than the angle of incidence β_1.

As a final remark, the scattering angle can also be in the same quadrant as the incident wave, i.e., $0<\beta_2<\pi/2$ (northeast). An example is shown in Fig. 10 where an incident wave of angle $\beta_1=\pi/6$ and wave number $k=2(\sqrt{3}+1)\pi/a_1$ is scattered by the reciprocal vector $\mathbf{K}_{-1,1}$ in a square lattice. The angle of the resonantly scattered wave is found to be $\beta_2=\pi/3$ from Eq. (5). The variations of the wave intensities are however similar, and will not be elaborated.

C. Backward scattering: cos $\beta_2<0$

1. The band gap

With $\cos\beta_2<0$, the discriminant (71) can have either sign depending on the magnitude of the detuning frequency Ω/Ω_0. It can be seen that $\Delta<0$ within the band gap defined by

$$\frac{\Omega_c^-}{\Omega_0}<\frac{\Omega}{\Omega_0}<\frac{\Omega_c^+}{\Omega_0}, \quad (90)$$

where

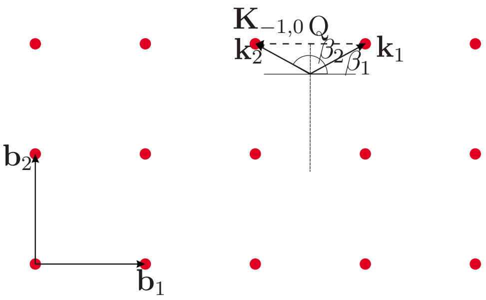

FIG. 11. (Color online) Backward Bragg scattering by the reciprocal vector $\mathbf{K}_{-1,0}$ in a square lattice of spacing a_1. The incident wave angle $\beta_1=\pi/6$ and the scattered wave angle $\beta_2=\pi-\beta_1=5\pi/6$. The wave number $k=2\pi/\sqrt{3}a_1$.

$$\frac{\Omega_c^{\mp}}{\Omega_0}=\frac{\cos\beta_2}{\cos(\beta_1-\beta_2)-1}\times\left(\mp\frac{|2\cos(\beta_1-\beta_2)-1|}{\sqrt{-\cos\beta_1\cos\beta_2}}-\frac{1}{2\cos\beta_1}+\frac{1}{2\cos\beta_2}\right). \quad (91)$$

Outside this band gap, $\Delta\geqslant 0$. The center of the band gap is at

$$\frac{\Omega_c^*}{\Omega_0}=\frac{\Omega_c^++\Omega_c^-}{2\Omega_0}=\frac{\cos\beta_2}{\cos(\beta_1-\beta_2)-1}\left(-\frac{1}{2\cos\beta_1}+\frac{1}{2\cos\beta_2}\right)=\frac{1}{2[1-\cos(\beta_1-\beta_2)]}\left(\frac{\cos\beta_2}{\cos\beta_1}-1\right) \quad (92)$$

and is always negative since $\cos\beta_2<0$. The width of the band gap is

$$\frac{\Omega_c^+-\Omega_c^-}{\Omega_0}=\frac{2\cos\beta_2}{\cos(\beta_1-\beta_2)-1}\frac{|2\cos(\beta_1-\beta_2)-1|}{\sqrt{-\cos\beta_1\cos\beta_2}}. \quad (93)$$

Within the band gap, the eigenvalues λ_1,λ_2 are complex conjugates of each other. Outside the band gap the eigenvalues are real.

As an example, we choose the square lattice of spacing a_1 and a horizontal reciprocal vector $\mathbf{K}_{-1,0}=-\mathbf{b}_1=-2\pi\mathbf{i}/a_1$, as shown in Fig. 11. Any point along the bisector of $\mathbf{K}_{-1,0}$ below point Q can be used as the vertex of a triangle whose two sides represent an incident wave vector $\mathbf{k}_1$ and a scattered wave vector $\mathbf{k}_2$. The scattered wave $\mathbf{k}_2$ is inclined at the angle $\beta_2=\pi-\beta_1$. We choose for demonstration $\beta_1=\pi/6$ so that $\beta_2=5\pi/6$ and the incident wave number is $k=2\pi/\sqrt{3}a_1$. It follows from Eq. (91) that the band gap boundaries are

$$\frac{\Omega_c^-}{\Omega_0}=-2,\quad \frac{\Omega_c^+}{\Omega_0}=\frac{2}{3}. \quad (94)$$

Since $\beta_2=\pi-\beta_1$, we get from Eqs. (68a) and (68d) that

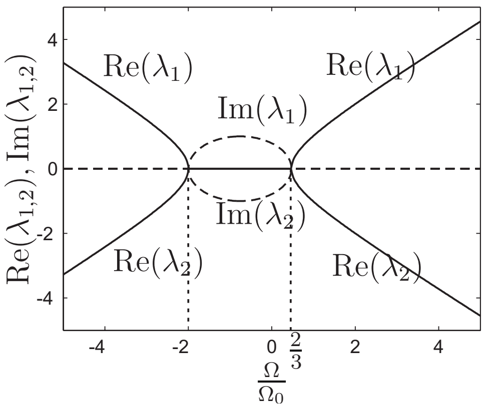

FIG. 12. Dependence of eigenvalues λ_1, λ_2 on detuning frequency Ω/Ω_0 for the backward-scattered waves shown in Fig. 11.

$$M_{11}+M_{22}=\frac{1}{2}\left(\frac{1}{\cos\beta_1}+\frac{1}{\cos\beta_2}\right)+\left(\frac{\Omega}{\Omega_0}\right)\left(\cos\beta_1+\frac{1-\sin\beta_1\sin\beta_2}{\cos\beta_2}\right)=0. \tag{95}$$

Therefore, Eq. (70) gives a pair of eigenvalues with opposite signs:

$$\lambda_{1,2}=\pm\frac{\Delta^{1/2}}{2}. \tag{96}$$

Within the band gap $-2<\Omega/\Omega_0<2/3$, $\Delta<0$, $\lambda_{1,2}=\pm i|\Delta|^{1/2}/2$ are purely imaginary. Outside the band gap $\Omega/\Omega_0<-2$ or $\Omega/\Omega_0>2/3$, $\Delta>0$, both eigenvalues are real. The computed values of λ_1 and λ_2 against the detuning Ω/Ω_0 are shown in Fig. 12.

2. Envelopes inside the strip

To complete the solution inside the strip, we impose the boundary conditions:

$$B_1(0)=1, \quad B_2(L)=0. \tag{97}$$

The solutions are

$$B_1(X)=\frac{e^{i\lambda_1\Omega_0X/C_g}}{1-e^{i\Delta^{1/2}\Omega_0L/C_g}\dfrac{M_{11}-\lambda_1}{M_{11}-\lambda_2}}+\frac{e^{i\lambda_2\Omega_0X/C_g}}{1-e^{-i\Delta^{1/2}\Omega_0L/C_g}\dfrac{M_{11}-\lambda_2}{M_{11}-\lambda_1}}, \tag{98a}$$

$$B_2(X)=-\frac{\dfrac{M_{11}-\lambda_1}{M_{12}}e^{i\lambda_1\Omega_0X/C_g}}{1-e^{i\Delta^{1/2}\Omega_0L/C_g}\dfrac{M_{11}-\lambda_1}{M_{11}-\lambda_2}}-\frac{\dfrac{M_{11}-\lambda_2}{M_{12}}e^{i\lambda_2\Omega_0X/C_g}}{1-e^{-i\Delta^{1/2}\Omega_0L/C_g}\dfrac{M_{11}-\lambda_2}{M_{11}-\lambda_1}}. \tag{98b}$$

To the left of the strip $X<0$, there is a reflected wave

$$B_2^-(X)=B_2(0)e^{i\mathcal{K}_2X}, \tag{99}$$

where $B_2(0)$ is found from Eq. (98b):

$$\begin{aligned}B_2(0)&=-\frac{\dfrac{M_{11}-\lambda_1}{M_{12}}}{1-e^{i\Delta^{1/2}\Omega_0L/C_g}\dfrac{M_{11}-\lambda_1}{M_{11}-\lambda_2}}-\frac{\dfrac{M_{11}-\lambda_2}{M_{12}}}{1-e^{-i\Delta^{1/2}\Omega_0L/C_g}\dfrac{M_{11}-\lambda_2}{M_{11}-\lambda_1}}\\&=-\frac{1}{M_{12}}\left\{\left(\frac{1}{M_{11}-\lambda_1}-\frac{e^{i\Delta^{1/2}\Omega_0L/C_g}}{M_{11}-\lambda_2}\right)^{-1}+\left(\frac{1}{M_{11}-\lambda_2}-\frac{e^{-i\Delta^{1/2}\Omega_0L/C_g}}{M_{11}-\lambda_1}\right)^{-1}\right\}.\end{aligned} \tag{100}$$

To the right of the strip $X>L$, there exists only the transmitted wave found from Eq. (65a)

$$B_1^+(X)=B_1^+(L)e^{i\mathcal{K}\cos\beta_1(X-L)}=B_1(L)e^{i\mathcal{K}\cos\beta_1(X-L)}, \tag{101}$$

by using the matching condition $B_1^+(L)=B_1(L)$ on the right boundary. The transmitted wave amplitude at $X=L$ is obtained from Eq. (98b):

$$B_1(L)=\frac{e^{i\lambda_1\Omega_0L/C_g}}{1-e^{i\Delta^{1/2}\Omega_0L/C_g}\dfrac{M_{11}-\lambda_1}{M_{11}-\lambda_2}}+\frac{e^{i\lambda_2\Omega_0L/C_g}}{1-e^{-i\Delta^{1/2}\Omega_0L/C_g}\dfrac{M_{11}-\lambda_2}{M_{11}-\lambda_1}}. \tag{102}$$

Again the two are related by energy conservation

$$|B_2(0)|^2=-\frac{\cos\beta_1}{\cos\beta_2}[1-|B_1(L)|^2]. \tag{103}$$

Figure 13 shows the spatial variation of the transmission intensity $|B_1(X)|^2$ and the reflection intensity $|B_2(X)|^2$ across the strip for various detunings $\Omega/\Omega_0=-3,0.5,2$. It follows from the energy conservation relation (76) and the relation $\beta_2=\pi-\beta_1$ that

$$\begin{aligned}&\cos\beta_1|B_1(X)|^2+\cos\beta_2|B_2(X)|^2\\&\quad=\cos\beta_1(|B_1(X)|^2-|B_2(X)|^2)=\text{const in }X,\end{aligned} \tag{104}$$

which implies that $|B_1(X)|^2-|B_2(X)|^2$ is the same for all X inside the strip, as can be seen in Fig. 13. The wave intensities are oscillatory in X for $\Omega/\Omega_0=-3$ and 2 which are outside the band gap, and attenuate monotonically for $\Omega/\Omega=0.5$ which is inside the band gap. Figure 14 (left) shows the dependence of reflection intensity at the incident edge $X=0$ on the detuning Ω/Ω_0 for different strip widths: $\Omega_0L/C_g=1,2,8$, while Fig. 14 (right) shows the transmission intensity at the exit edge $X=L$. Clearly transmission through the strip decreases rapidly when the detuning frequency is inside the band gap $-2<\Omega/\Omega_0<2/3$, and the minimum is smaller for a wider strip. Outside the band gap, the transmission

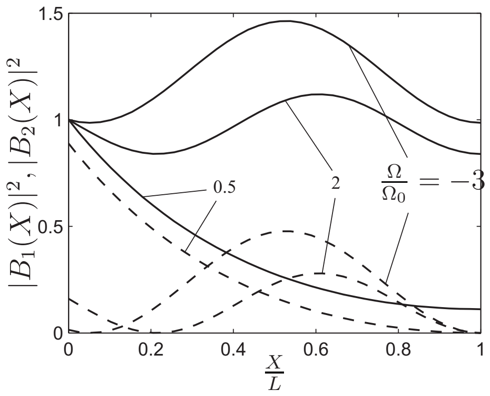

FIG. 13. Spatial distribution of the scattered wave intensities across the strip for the scattering configuration in Fig. 11. Detuning frequencies are $\Omega/\Omega_0=-3,2$ (outside the band gap) and $\Omega/\Omega_0=0.5$ (inside the band gap). The dimensionless strip length is $\Omega_0 L/C_g=2$. Solid curves, transmission intensity $|B_1(X)|^2$; dashed curves, reflection intensity $|B_2(X)|^2$.

intensity oscillates with respect to the detuning frequency. Consistent with energy conservation (103), the reflection intensity at $X=0$ becomes large when Ω/Ω_0 is inside the band gap and increases with increasing strip width. When $\Omega_0 L/C_g=8$, reflection is nearly total and transmission is essentially zero.

VII. TWO SCATTERED WAVES

A. Coupled-mode equations and boundary conditions for the wave envelopes

Next in complexity is the case of three-wave resonance involving one incident and two scattered waves. In accordance with Ewald procedure, if a circle can be drawn to pass three noncollinear nodes P_j, $j=1,2,3$ in the reciprocal lattice, then $\mathbf{k}_j=\overrightarrow{OP_j}$ are the three wave vectors having the same k. One of them with angle between $(0,\pi/2)$ will be designated as the incident wave $\mathbf{k}_1$. The vector difference of any two is a reciprocal lattice vector.

Three types of scattering are possible.

(1) Type I (forward-forward): Both resonated waves $\mathbf{k}_2$ and $\mathbf{k}_3$ are scattered forward as shown in Fig. 15(a). The directional cosines are $\cos\beta_2>0$, $\cos\beta_3>0$. This case is similar to Laue-Laue scattering in x-ray crystallography [43].

(2) Type II (forward-backward): One resonated wave $\mathbf{k}_2$ is reflected and the other $\mathbf{k}_3$ is scattered forward, shown in Fig. 15(b). The direction cosines $\cos\beta_2<0$, $\cos\beta_3>0$. This case is similar to Laue-Bragg scattering in crystallography.

(3) Type III (backward-backward): Both resonated waves are reflected, as shown in Fig. 15(c). The direction cosines $\cos\beta_2<0$, $\cos\beta_3<0$. This case is similar to Bragg-Bragg scattering in crystallography.

For the given incident wave envelope

$$A_1^- = A_0 e^{i(\mathcal{K}\cos\beta_1 X + \mathcal{K}\sin\beta_1 Y - \Omega T)} \tag{105}$$

we let the wave envelopes in the three regions be

$$\begin{bmatrix} A_j^- \\ A_j \\ A_j^+ \end{bmatrix} = \begin{bmatrix} B_j^-(X) \\ B_j(X) \\ B_j^+(X) \end{bmatrix} A_0 e^{i(\mathcal{K}\sin\beta_1 Y - \Omega T)}, \qquad \begin{matrix} -\infty < X < 0, \\ 0 \leq X \leq L, \\ L < X < \infty, \end{matrix} \tag{106}$$

where $j=1,2,3$. It follows from Eq. (45) that outside the strip, the factors $B_j^{\mp}$ are governed by the uncoupled equations

$$\frac{dB_j^{\mp}}{dX} = \frac{i\mathcal{K}(1-\sin\beta_1\sin\beta_j)}{\cos\beta_j} B_j^{\mp}, \quad j=1,2,3. \tag{107}$$

Within the strip $0 \leq X \leq L$, the three waves are coupled by the third-order differential system

$$\frac{d}{dX}\begin{bmatrix} B_1 \\ B_2 \\ B_3 \end{bmatrix} = \frac{i\Omega_0}{C_g}\mathbf{M}\begin{bmatrix} B_1 \\ B_2 \\ B_3 \end{bmatrix}, \tag{108}$$

where $\mathbf{M}$ is a 3×3 matrix with entries given by

$$M_{jj} = \frac{1}{2\cos\beta_j} + \left(\frac{\Omega}{\Omega_0}\right)\frac{1-\sin\beta_1\sin\beta_j}{\cos\beta_j}, \quad j=1,2,3, \tag{109a}$$

$$M_{j\ell} = \frac{2\cos(\beta_j-\beta_\ell)-1}{2\cos\beta_j}, \quad j \neq \ell. \tag{109b}$$

In the open waters, the solutions of $B_j^{\mp}$ are

$$B_j^-(X) = B_j^-(0)\exp\left[\frac{i\mathcal{K}(1-\sin\beta_1\sin\beta_j)X}{\cos\beta_j}\right], \quad X<0, \tag{110a}$$

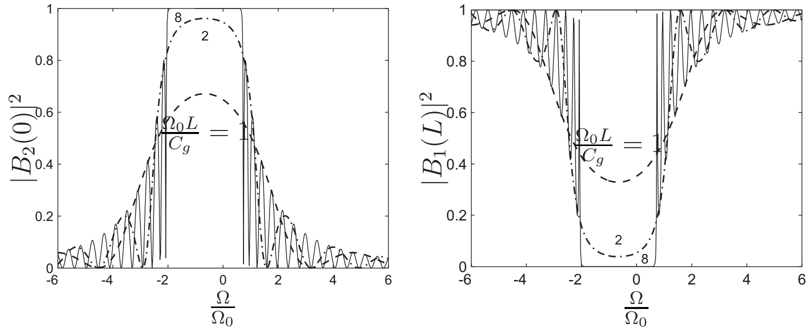

FIG. 14. Reflection intensity $|B_2(0)|^2$ at the incident edge of strip (left), and transmission intensity $|B_1(L)|^2$ at the exit edge of strip (right) for various detuning Ω/Ω_0 and strip widths. Dashed curve, $\Omega_0 L/C_g=1$; dash-dot curve, $\Omega_0 L/C_g=2$; solid curve, $\Omega_0 L/C_g=8$. Configuration of Bragg scattering is shown in Fig. 11.

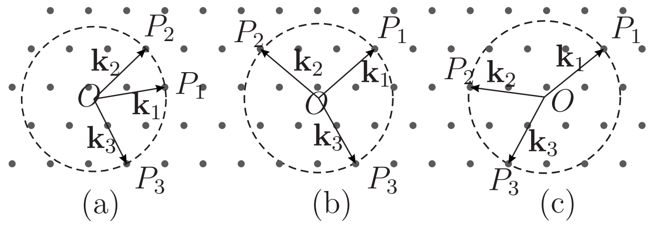

FIG. 15. Three types of three-wave Bragg resonance: (a) Both $\mathbf{k}_2$ and $\mathbf{k}_3$ are scattered forward; (b) $\mathbf{k}_2$ is reflected and $\mathbf{k}_3$ is scattered forward; (c) both $\mathbf{k}_2$ and $\mathbf{k}_3$ are reflected.

$$B_j^+(X)=B_j^+(L)\exp\left[\frac{i\mathcal{K}(1-\sin\beta_1\sin\beta_j)(X-L)}{\cos\beta_j}\right],\quad X>L. \tag{110b}$$

The direction of the envelope of the jth scattered wave is

$$\varphi_j=\tan^{-1}\frac{\mathcal{K}\sin\beta_1}{\mathcal{K}\dfrac{1-\sin\beta_1\sin\beta_j}{\cos\beta_j}}=\tan^{-1}\left(\frac{\sin\beta_1\cos\beta_j}{1-\sin\beta_1\sin\beta_j}\right),\quad j=2,3, \tag{111}$$

which is in general different from the direction of the wave vector $\mathbf{k}_j$. Since

$$\left|\frac{\tan\beta_j}{\tan\beta_1}\right|=\left|\frac{\sin\beta_1\cos\beta_j}{1-\sin\beta_1\sin\beta_j}\frac{\cos\beta_1}{\sin\beta_1}\right|=\left|\frac{\cos\beta_1\cos\beta_j}{1-\sin\beta_1\sin\beta_j}\right|\leqslant 1, \tag{112}$$

the angles of scattered wave envelopes (hence energy) are smaller than the angle of the transmitted wave $\varphi_1=\beta_1$.

Inside the strip $0\leqslant X\leqslant L$, the general solution of Eq. (110) is of the form

$$\mathbf{B}\equiv[B_1,B_2,B_3]^T=C_1\mathbf{V}^{(1)}e^{i\lambda_1\Omega_0X/C_g}+C_2\mathbf{V}^{(2)}e^{i\lambda_2\Omega_0X/C_g}+C_3\mathbf{V}^{(3)}e^{i\lambda_3\Omega_0X/C_g}, \tag{113}$$

where λ_j and $\mathbf{V}^{(j)}, j=1,2,3$ are the *distinct* eigenvalues and the corresponding eigenvectors of the matrix $\mathbf{M}$, respectively. The coefficients C_j, $j=1,2,3$ will be determined by boundary conditions at the edges of the cylinder strip. If two or three eigenvalues are equal, the solution assumes a different form; these special cases will not be pursued.

The eigenvalues condition

$$\det(\lambda\mathbf{I}_{3\times3}-\mathbf{M})=0, \tag{114}$$

is equivalent to the cubic equation

$$\lambda^3+\alpha_2\lambda^2+\alpha_1\lambda+\alpha_0=0, \tag{115}$$

with the coefficients

$$\alpha_2=-(M_{11}+M_{22}+M_{33}), \tag{116a}$$

$$\alpha_1=\det\left(\begin{bmatrix}M_{11} & M_{12}\\ M_{21} & M_{22}\end{bmatrix}\right)+\det\left(\begin{bmatrix}M_{11} & M_{13}\\ M_{31} & M_{33}\end{bmatrix}\right)+\det\left(\begin{bmatrix}M_{22} & M_{23}\\ M_{32} & M_{33}\end{bmatrix}\right), \tag{116b}$$

$$\alpha_0=-\det(\mathbf{M}). \tag{116c}$$

The reality of the eigenvalues λ_j, $j=1,2,3$, depends on the sign of the following discriminant (Sec. 3.8.2 in [45]):

$$\Delta_3=4\alpha_1^3-\alpha_1^2\alpha_2^2+4\alpha_0\alpha_2^3-18\alpha_0\alpha_1\alpha_2+27\alpha_0^2, \tag{117}$$

which is a function of the detuning frequency Ω/Ω_0. If $\Delta_3\leqslant 0$, all three eigenvalues are real. The eigensolutions (113) are oscillatory in X with wave number $\lambda_1\Omega_0/C_g$, $\lambda_2\Omega_0/C_g$ and $\lambda_3\Omega_0/C_g$ and have constant amplitudes. If $\Delta_3>0$, only one eigenvalue is real and the other two are complex conjugates. Only one of eigensolution (113) is oscillatory in X with constant amplitude. The remaining two are oscillatory with exponentially decaying or growing amplitude; waves are evanescent. Corresponding to the eigenvalue λ_j, the eigenvector is

$$\mathbf{V}^{(j)}=[V_1^{(j)},V_2^{(j)},V_3^{(j)}]^T=\begin{bmatrix}\lambda_jM_{13}+M_{12}M_{23}-M_{13}M_{22}\\ \lambda_jM_{23}+M_{13}M_{21}-M_{11}M_{23}\\ (\lambda_j-M_{11})(\lambda_j-M_{22})-M_{12}M_{21}\end{bmatrix},\quad j=1,2,3. \tag{118}$$

For the three types of scattering configuration, the following boundary conditions are needed to find the coefficients C_1, C_2, and C_3.

(1) Type I: Forward-forward scattering

$$B_1(0)=1,\quad B_2(0)=0,\quad B_3(0)=0. \tag{119}$$

Mathematically, these amount to initial conditions.

(2) Type II: Forward-backward scattering

$$B_1(0)=1,\quad B_2(L)=0,\quad B_3(0)=0. \tag{120}$$

Here $B_2(X)$ denotes the backward-scattered wave and $B_3(X)$ the forward-scattered.

(3) Type III: Backward-backward scattering

$$B_1(0)=1,\quad B_2(L)=0,\quad B_3(L)=0. \tag{121}$$

We shall examine each of the three types separately. For checking the correctness of calculations it is useful to make use of the law of wave energy conservation (47) which can be integrated to give

$$\sum_{j=1}^{3}\cos\beta_j|B_j(X)|^2=\sum_{j=1}^{3}\cos\beta_j|B_j(0)|^2=\sum_{j=1}^{3}\cos\beta_j|B_j(L)|^2 \tag{122}$$

applicable equally to all three types.

B. Type I: Forward-forward scattering

As the first example, let us consider a rectangular lattice of x spacing a_1 and y spacing $a_1/2$. The primitive vectors of

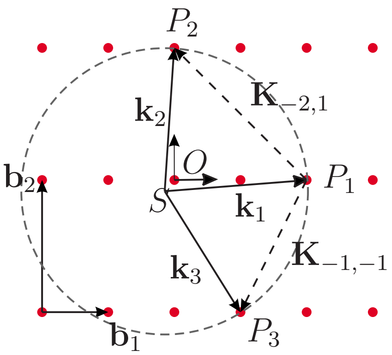

FIG. 16. (Color online) Configuration in the reciprocal lattice for type I (forward-forward) scattering. The direct primitive vectors are $\mathbf{a}_1=a_1\mathbf{i}$ and $\mathbf{a}_2=\frac{1}{2}a_1\mathbf{j}$. The reciprocal primitive vectors are $\mathbf{b}_1=2\pi\mathbf{i}/a_1$ and $\mathbf{b}_2=4\pi\mathbf{j}/a_1$. The resonated wave vectors are $\mathbf{k}_1=(13\pi/3a_1)\mathbf{i}+(\pi/3a_1)\mathbf{j}$, $\mathbf{k}_2=(1\pi/3a_1)\mathbf{i}+(13\pi/3a_1)\mathbf{j}$, and $\mathbf{k}_3=(7\pi/3a_1)\mathbf{i}+(11\pi/3a_1)\mathbf{j}$. The wave number at resonance is $k=\sqrt{170}\pi/3a_1$.

the reciprocal lattice space is $\mathbf{b}_1=2\pi\mathbf{i}/a_1$ and $\mathbf{b}_2=4\pi\mathbf{j}/a_1$. In Fig. 16, the reciprocal lattice and the Ewald circle passing three nodes P_1, P_2, and P_3 are shown, where $\overrightarrow{P_1P_2}=\mathbf{K}_{-2,1}$ and $\overrightarrow{P_1P_3}=\mathbf{K}_{-1,-1}$ are the reciprocal lattice vectors of Bragg resonance. The center of the Ewald circle (point S) can be found by solving $|\overrightarrow{SP_1}|=|\overrightarrow{SP_2}|=|\overrightarrow{SP_3}|$, where the vectors from point O are $\overrightarrow{OP_1}=2\mathbf{b}_1$, $\overrightarrow{OP_2}=\mathbf{b}_2$, and $\overrightarrow{OP_3}=\mathbf{b}_1-\mathbf{b}_2$, respectively. It can be easily found that the center S is located at $\overrightarrow{OS}=(-\pi\mathbf{i}/3a_1,-\pi\mathbf{j}/3a_1)$; the magnitude of $\mathbf{k}_j$ is

$$k=|\overrightarrow{SP_1}|=|\overrightarrow{OP_1}-\overrightarrow{OS}| = \sqrt{\left[\frac{4\pi}{a_1}-\left(-\frac{\pi}{3a_1}\right)\right]^2+\left[0-\left(-\frac{\pi}{3a_1}\right)\right]^2}=\frac{\sqrt{170}\pi}{3a_1}. \tag{123}$$

The directions of $\mathbf{k}_1$, $\mathbf{k}_2$, and $\mathbf{k}_3$ are easily found:

$$\beta_1=\arg(\overrightarrow{SP_1})=\tan^{-1}\frac{1}{13}\approx 4.4\,^\circ,$$

$$\beta_2=\arg(\overrightarrow{SP_2})=\tan^{-1}13\approx 85.6\,^\circ,$$

$$\beta_3=\arg(\overrightarrow{SP_3})=-\tan^{-1}\frac{11}{7}\approx -57.53\,^\circ. \tag{124}$$

With these results the discriminant (117) is plotted against the detuning parameter Ω/Ω_0 in Fig. 17. The corresponding three eigenvalues are plotted in Fig. 18. For all detuning frequencies, the discriminant is negative, hence all three eigenvalues are real. The coefficients in Eq. (113) can be found from the boundary (or, rather, initial) conditions (119), all imposed on the left side $X=0$. The results are

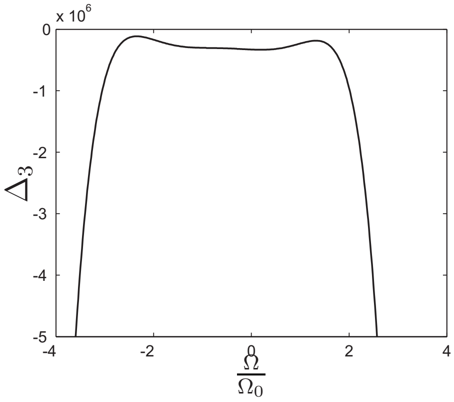

FIG. 17. Discriminant (117) for type I scattering shown in Fig. 16.

$$\begin{bmatrix} C_1 \\ C_2 \\ C_3 \end{bmatrix} = \frac{\begin{bmatrix} V_2^{(2)}V_3^{(3)}-V_2^{(3)}V_3^{(2)} \\ V_2^{(3)}V_3^{(1)}-V_2^{(1)}V_3^{(3)} \\ V_2^{(1)}V_3^{(2)}-V_2^{(2)}V_3^{(1)} \end{bmatrix}}{\det\begin{bmatrix} V_1^{(1)} & V_1^{(2)} & V_1^{(3)} \\ V_2^{(1)} & V_2^{(2)} & V_2^{(3)} \\ V_3^{(1)} & V_3^{(2)} & V_3^{(3)} \end{bmatrix}}, \tag{125}$$

where $\mathbf{V}^{(j)}$ is defined in Eq. (118).

For better understanding of the derived result, we first display in Fig. 19 the three coefficients for the transmitted wave: $C_1V_1^{(1)}$, $C_2V_1^{(2)}$, and $C_3V_1^{(3)}$, which appear in Eq. (113), for a range of detuning parameter Ω/Ω_0. Since the solution is determined only by the initial values at $X=0$, the results are independent of L, i.e., the strip width can be terminated at any X.

Figure 20 shows the spatial variation of the energy intensities of the transmitted wave $|B_1(X)|^2$ and of the two forward-scattered waves $|B_2(X)|^2$ and $|B_3(X)|^2$ for a range of detuning frequencies Ω/Ω_0. We stress that the width of the strip can be different from the extent of the plot, $0\leqslant X\leqslant 10$. When the detuning is large, such as $\Omega/\Omega_0=-4.30$, -3.35, and 2.35, transmission is nearly perfect and scattering is

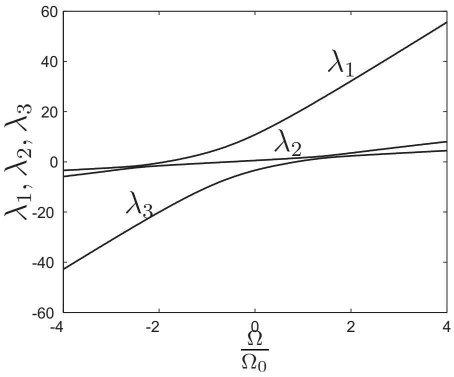

FIG. 18. Three eigenvalues in type I (forward-forward) scattering for the geometry shown in Fig. 16.

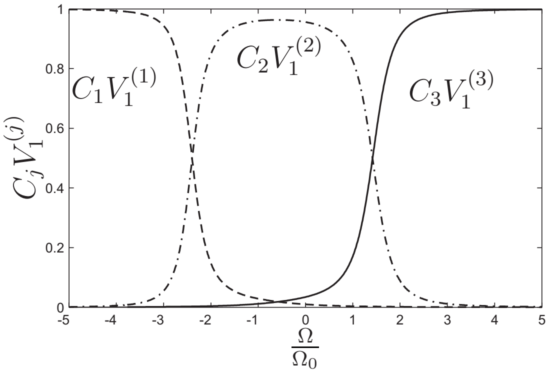

FIG. 19. Three coefficients of the transmitted wave in type I scattering shown in Fig. 16.

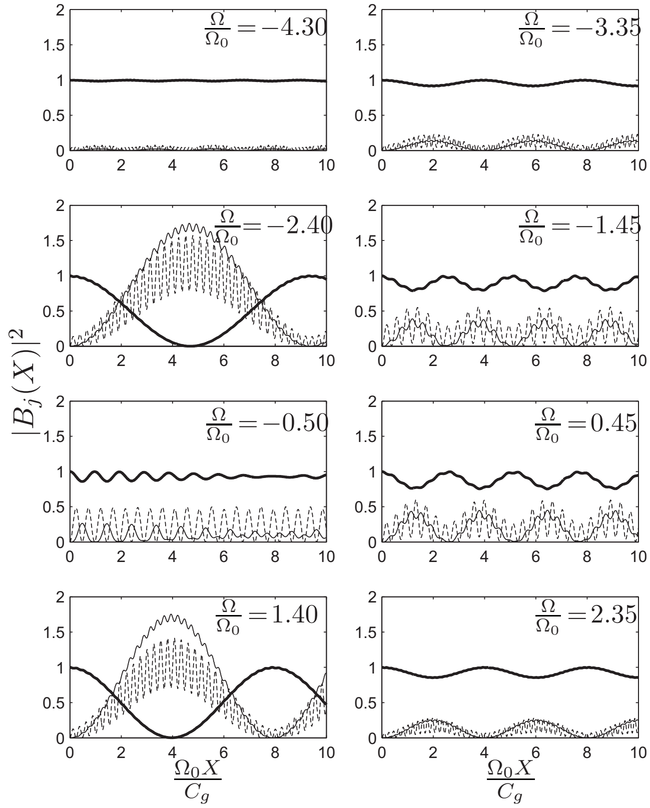

FIG. 20. Variation of wave intensities $|B_j(X)|^2$, $j=1,2,3$ along the strip for various detuning Ω/Ω_0 of type I forward-forward scattering in Fig. 16. Thick solid curve, $|B_1(X)|^2$; dashed curve, $|B_2(X)|^2$; thin solid curve, $|B_3(X)|^2$.

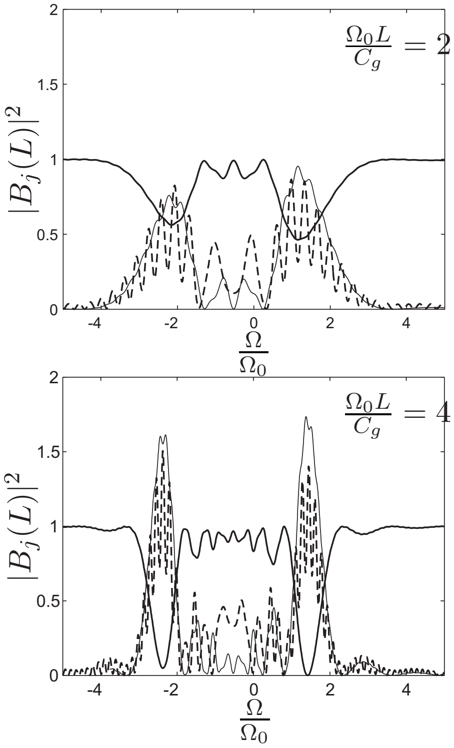

FIG. 21. Dependence of wave intensities for type I Bragg scattering on the detuning frequency Ω/Ω_0 for two strip widths $\Omega_0L/C_g=2$ (top) and $\Omega_0L/C_g=4$ (bottom). Thick solid curve, $|B_1(L)|^2$; dashed curve, $|B_2(L)|^2$; thin solid curve, $|B_3(L)|^2$. The geometry of waves in the reciprocal lattice is shown in Fig. 16.

weak. $|B_j(X)|^2$ oscillates with X sinusoidally according to Eq. (113). The amplitudes of the forward-scattered waves become significant only for smaller detuning $\Omega/\Omega_0=-1.45$, -0.50 and 0.45. When $\Omega/\Omega_0=-2.40$, the transmission wave vanishes at $\Omega_0X/C_g\approx 4.70$ while the scattered waves are the greatest. Thus the strip length and detuning frequency can be so chosen as to convert most of the incident wave energy to scattered waves at the exit. Since $\sin\beta_2>0$ and $\sin\beta_3<0$, $\mathbf{k}_2$ corresponds to positive forward scattering (northeast), and $\mathbf{k}_3$ to negative (southeast) forward scattering. Similar result is found for $\Omega/\Omega_0=1.40$ at $\Omega_0X/C_g\approx 4.0$. Note in Fig. 18 and Fig. 19 that, near $\Omega/\Omega_0=-2.40$, the coefficients $C_1V_1^{(1)}$ and $C_2V_1^{(2)}$ are very nearly the same and equal to 0.50. The eigenvalues λ_1 and λ_2 are also close to each other. On the other hand, the third coefficient $C_3V_1^{(3)}$ is nearly zero. Therefore, the transmitted wave B_1 is dominated by the first two eigenvectors; its intensity can be approximated by

$$\begin{aligned}|B_1(X)|^2 &\sim |C_1V_1^{(1)}e^{i\lambda_1\Omega_0X/C_g}+C_2V_1^{(2)}e^{i\lambda_2\Omega_0X/C_g}|^2\\ &\sim \frac{1}{4}|1+e^{i(\lambda_2-\lambda_1)\Omega_0X/C_g}|^2\\ &=\cos^2\frac{(\lambda_1-\lambda_2)\Omega_0X}{2C_g}. \qquad (126)\end{aligned}$$

At $\Omega/\Omega_0=-2.40$, the first two eigenvalues are $\lambda_1=-1.494$ and $\lambda_2=-2.1634$. It follows from Eq. (126) that the minimum transmitted wave amplitude occurs around $\Omega_0X/C_g=\pi/(\lambda_1-\lambda_2)=4.6931$ as seen in Fig. 20. Similar approximation also predicts the oscillatory variation of $|B_1(X)|^2$ at $\Omega/\Omega_0=1.40$. Since $C_2V_1^{(2)}\approx C_3V_1^{(3)}\approx\frac{1}{2}$, $C_1V_1^{(1)}\approx 0$ and $\lambda_2=2.2166$, $\lambda_3=1.4253$. Similar to Eq. (126), the first minimum transmission intensity occurs around $\Omega_0X/C_g=\pi/(\lambda_2-\lambda_3)=3.97$, as is indeed shown in Fig. 20.

Figure 21 shows the dependence of the transmitted and scattered wave intensities on the detuning frequency for two different strip widths $\Omega_0L/C_g=2$ and 4. There are two nar-

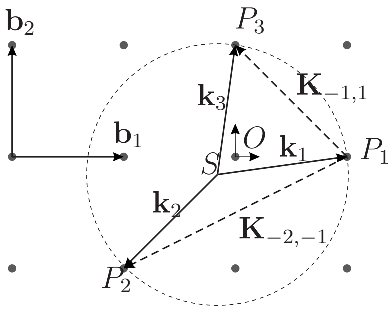

FIG. 22. Type II Bragg resonance in a square lattice of primitive vectors $\mathbf{a}_1 = a_1\mathbf{i}$ and $\mathbf{a}_2 = a_1\mathbf{j}$. The primitive reciprocal vectors are $\mathbf{b}_1 = 2\pi\mathbf{i}/a_1$ and $\mathbf{b}_2 = 2\pi\mathbf{j}/a_1$. The resonated wave vectors are $\mathbf{k}_1 = (7\pi/3a_1)\mathbf{i} + (\pi/3a_1)\mathbf{j}$, $\mathbf{k}_2 = -(5\pi/3a_1)\mathbf{i} - (5\pi/3a_1)\mathbf{j}$, and $\mathbf{k}_3 = (\pi/3a_1)\mathbf{i} + (7\pi/3a_1)\mathbf{j}$. The wave number at resonance is $k = 5\sqrt{2}\pi/3a_1$.

row valleys near $\Omega/\Omega_0 \approx -2.4$ and $\Omega/\Omega_0 \approx 1.4$ where transmission at the exit edge is weak and scattering is strong. These results can be better understood by the coefficients shown in Fig. 19. Away from the center of a valley, $|B_1(L)|$ is approximately unity, being dominated by just one of the coefficients $C_1V_1^{(1)}$, $C_1V_1^{(2)}$, or $C_1V_1^{(3)}$. Near the center of a valley, the transmission intensity can be estimated by Eq. (126). Thus for $\Omega/\Omega_0 \approx -2.40$, one finds $\lambda_1 = -1.494, \lambda_2 = -2.1634$ from Fig. 18; hence

$$|B_1(L)|^2 \approx \left| \cos \frac{(\lambda_1 - \lambda_2)}{2} \frac{\Omega_0 L}{C_g} \right|^2 = \begin{cases} 0.6150, & \dfrac{\Omega_0 L}{C_g} = 2 \\ 0.0529, & \dfrac{\Omega_0 L}{C_g} = 4. \end{cases}$$

For $\Omega/\Omega_0 = 1.4$, one finds $\lambda_2 = 2.2166$ and $\lambda_3 = 1.4253$; hence

$$|B_1(L)|^2 \approx \left| \cos \frac{(\lambda_2 - \lambda_3)}{2} \frac{\Omega_0 L}{C_g} \right|^2 = \begin{cases} 0.4941, & \dfrac{\Omega_0 L}{C_g} = 2 \\ 0.0001, & \dfrac{\Omega_0 L}{C_g} = 4. \end{cases}$$

These estimates agree well with the numerical result in Fig. 21. From the preceding formulas, the valley on the left is the deepest if the strip width is such that $\Omega_0 L/C_g = (2n+1)\pi/(\lambda_1 - \lambda_2)$, $n = 0, 1, \ldots$, corresponding to vanishing transmission. The valley disappears if for $\Omega_0 L/C_g = 2n\pi/(\lambda_1 - \lambda_2)$, $n = 0, 1, \ldots$. By replacing $\lambda_1 - \lambda_2$ with $\lambda_2 - \lambda_3$, the same results held for the valley on the right.

C. Type II: Forward-backward scattering

For this example, we choose a square lattice of spacing a_1. The Ewald circle passing the three nodes P_1, P_2, and P_3 in the reciprocal lattice is shown in Fig. 22, where $\overrightarrow{P_1P_3} = \mathbf{K}_{-1,1}$ and $\overrightarrow{P_1P_2} = \mathbf{K}_{-2,-1}$. The coordinates of the center S of the Ewald circle can be found by solving $|\overrightarrow{SP_1}| = |\overrightarrow{SP_2}| = |\overrightarrow{SP_3}|$, where the nodes P_1, P_2, P_3 are located at $\mathbf{b}_1$, $-(\mathbf{b}_1 + \mathbf{b}_2)$, and $\mathbf{b}_2$, respectively. The center S is found to be at $\overrightarrow{OS} = (-\pi\mathbf{i}/3a_1, -\pi\mathbf{j}/3a_1)$. Thus the wave number at resonance is

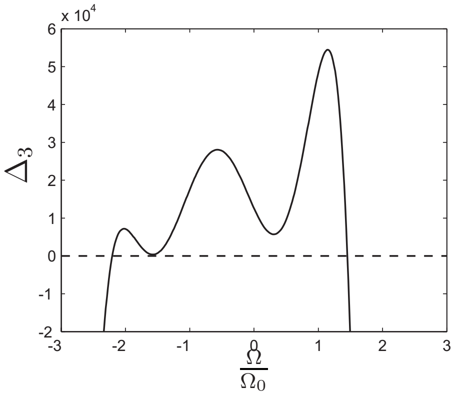

FIG. 23. Discriminant (117) for type II forward-backward scattering. The resonated wave vectors are shown in Fig. 22.

$$k = |\overrightarrow{SP_1}| = \sqrt{\left[\frac{2\pi}{a_1} - \left(-\frac{\pi}{3a_1}\right)\right]^2 + \left[0 - \left(-\frac{\pi}{3a_1}\right)\right]^2} = \frac{5\sqrt{2}\pi}{3a_1}. \tag{127}$$

The corresponding angles of $\mathbf{k}_1$, $\mathbf{k}_2$, and $\mathbf{k}_3$ are

$$\beta_1 = \arg(\overrightarrow{SP_1}) = \tan^{-1}\frac{1}{7} \approx 8.13°,$$

$$\beta_2 = \arg(\overrightarrow{SP_2}) = -\frac{3\pi}{4} = -135°,$$

$$\beta_3 = \arg(\overrightarrow{SP_3}) = \tan^{-1} 7 \approx 81.87°. \tag{128}$$

As shown in Fig. 23 the discriminant Δ_3 according to Eq. (117) is positive within the band gap $-2.2056 < \Omega/\Omega_0 < 1.4516$ and negative outside. Within the band gap the eigenvalue λ_3 is real and λ_1, λ_2 are complex conjugates, as shown in Fig. 24. By imposing the boundary conditions (120), the coefficients C_j are found:

$$\begin{bmatrix} C_1 \\ C_2 \\ C_3 \end{bmatrix} = \frac{\begin{bmatrix} e^{i\lambda_2\Omega_0 L/C_g}V_2^{(2)}V_3^{(3)} - e^{i\lambda_3\Omega_0 L/C_g}V_2^{(3)}V_3^{(2)} \\ e^{i\lambda_3\Omega_0 L/C_g}V_2^{(3)}V_3^{(1)} - e^{i\lambda_1\Omega_0 L/C_g}V_2^{(1)}V_3^{(3)} \\ e^{i\lambda_1\Omega_0 L/C_g}V_2^{(1)}V_3^{(2)} - e^{i\lambda_2\Omega_0 L/C_g}V_2^{(2)}V_3^{(1)} \end{bmatrix}}{\det\begin{bmatrix} V_1^{(1)} & V_1^{(2)} & V_1^{(3)} \\ e^{i\lambda_1\Omega_0 L/C_g}V_2^{(1)} & e^{i\lambda_2\Omega_0 L/C_g}V_2^{(2)} & e^{i\lambda_3\Omega_0 L/C_g}V_2^{(3)} \\ V_3^{(1)} & V_3^{(2)} & V_3^{(3)} \end{bmatrix}}. \tag{129}$$

Figure 25 shows the moduli of the three coefficients for the transmitted wave: $C_1V_1^{(1)}$, $C_2V_1^{(2)}$, and $C_3V_1^{(3)}$. At the boundaries of the band gap (see Fig. 24), the first two eigenvalues coalesce, $\lambda_1 \to \lambda_2^*$; hence $\mathbf{V}^{(1)} \to \mathbf{V}^{(2)}$. The denominator of Eq.

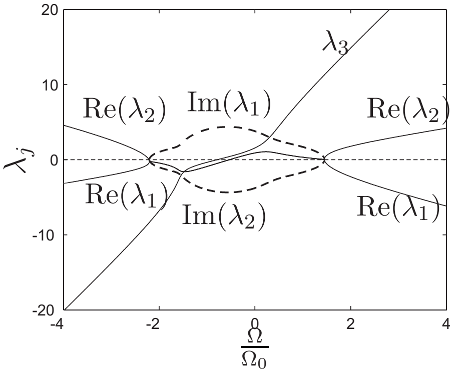

FIG. 24. Three eigenvalues for type II forward-backward scattering shown in Fig. 22. Solid curves are for the real parts and dashed curves are for the imaginary parts of eigenvalues.

(129) tends to zero and the coefficients become unbounded, as displayed in Fig. 25. In principle, a finite solution different in form from Eq. (113) can be found, but is omitted here. Outside the band gap, all three eigensolutions are oscillatory in X but their relative magnitudes are different, as can be seen from Fig. 25.

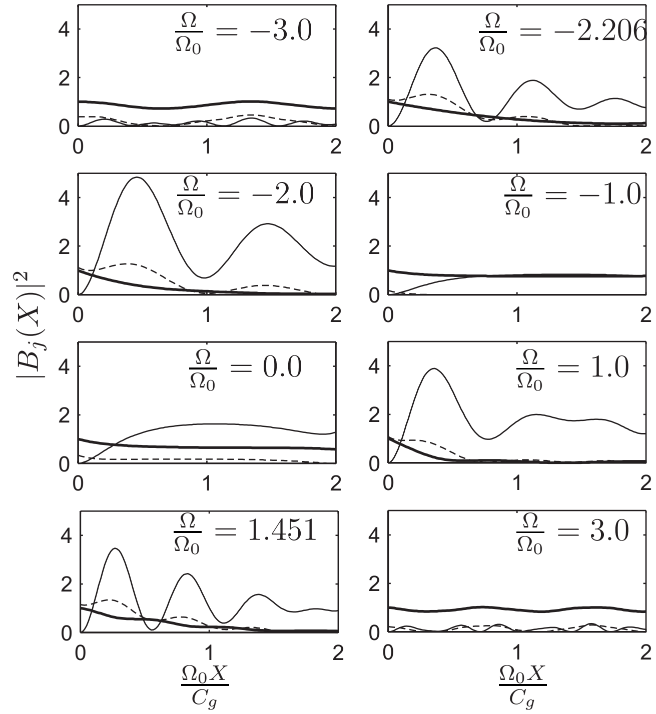

FIG. 26. Variation of wave intensities across the strip in type II scattering, for different Ω/Ω_0. Strip width is $\Omega_0 L/C_g=2$. Thick solid curve, $|B_1(X)|^2$ (transmitted); dashed curve, $|B_2(X)|^2$ (reflected); thin solid curve, $|B_3(X)|^2$ (scattered forward). The reciprocal lattice and wave vectors are shown in Fig. 22.

Figure 26 shows the spatial variation of the wave intensities $|B_1(X)|^2$, $|B_2(X)|^2$, and $|B_3(X)|^2$ across a strip of width $\Omega_0 L/C_g=2$. When the detuning is $\Omega/\Omega_0=-3.0, 3.0$, hence large and outside the band gap, the scattered waves $|B_2(X)|^2$ and $|B_3(X)|^3$ are both weak. $|B_1(X)|$ is close to unity. These are consistent with the coefficients shown in Fig. 25. Inside but close to the borders of the band gap, when $\Omega/\Omega_0 \approx -2.0, 1.0$, $|C_1V_1^{(1)}| \approx 1$, and $|C_2V_1^{(2)}|$, $|C_3V_1^{(3)}| \approx 0$. Thus the transmitted wave $|B_1(X)|^2$ consists mainly of eigenfunction $\exp(i\lambda_1\Omega_0 X/C_g)$, which attenuates along X due to $\mathrm{Im}(\lambda_1)>0$. In the central region within the band gap, $\Omega/\Omega_0=-1.0, 0.0$, $|C_1V_1^{(1)}|$ is small but finite, $|C_2V_1^{(2)}|\approx 0$ and $|C_3V_1^{(3)}|\approx 1$. The transmitted wave intensity consists of a large harmonic component of (nearly) unit amplitude and a small spatially decaying component, as shown in Fig. 26. Since $\lambda_3 \approx 0$, the forward-scattered wave $|B_3(X)|^2$ is essentially uniform along X except near the left entry of the strip. The reflected wave intensity $|B_2(X)|^2$ is weak. Near the borders of the band gap, $\Omega/\Omega_0=-2.206, 1.451$ where Δ_3 becomes very small, the attenuation of $|B_1(X)|^2$ becomes nearly linear along X. This is to be expected since $\lambda_1 \approx \lambda_2$, and $|C_3V_1^{(3)}| \approx 0$.

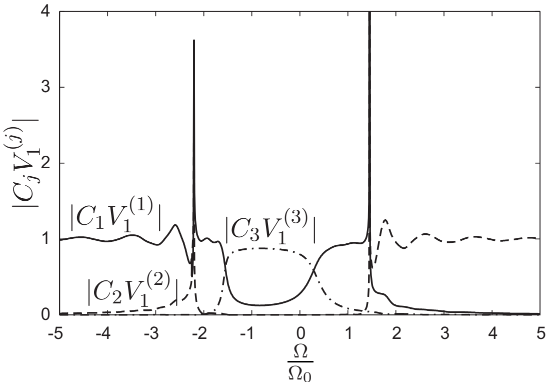

FIG. 25. Moduli of the three coefficients of the transmitted wave in type II scattering for the configuration shown in Fig. 22. Solid curve, $C_1V_1^{(1)}$; dashed curve, $C_2V_1^{(2)}$; dash-dot curve, $C_3V_1^{(3)}$.

The dependence of the wave intensities on the detuning frequency is displayed in Fig. 27 for a strip of width $\Omega_0 L/C_g=2$. In the range where $\Delta_3<0$, the dependence of intensities on Ω/Ω_0 is oscillatory. For large detuning, both forward-scattered $|B_3(L)|^2$ and backscattered $|B_2(0)|^2$ waves

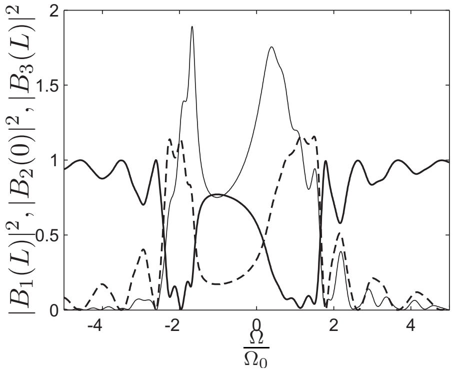

FIG. 27. Dependence of wave intensities in type II scattering on the detuning frequency Ω/Ω_0 for $\Omega_0 L/C_g=2$. Heavy solid curve, $|B_1(L)|^2$ (transmitted); dashed curve, $|B_2(0)|^2$ (reflected); thin solid curve, $|B_3(L)|^2$ (scattered forward). The reciprocal lattice and wave vectors are shown in Fig. 22.

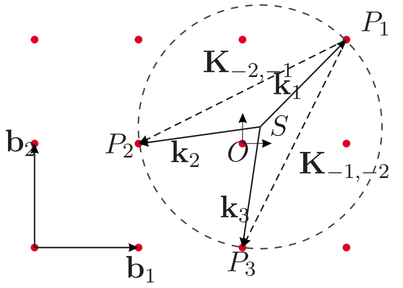

FIG. 28. (Color online) Type III scattering in a square lattice of primitive vectors $\mathbf{a}_1 = a_1\mathbf{i}$ and $\mathbf{a}_2 = a_1\mathbf{j}$. The primitive vectors of the reciprocal lattice are $\mathbf{b}_1 = 2\pi\mathbf{i}/a_1$ and $\mathbf{b}_2 = 2\pi\mathbf{j}/a_1$. The resonated wave vectors $\mathbf{k}_1 = (5\pi/3a_1)\mathbf{i} + (5\pi/3a_1)\mathbf{j}$, $\mathbf{k}_2 = -(7\pi/3a_1)\mathbf{i} - (\pi/3a_1)\mathbf{j}$, and $\mathbf{k}_3 = -(\pi/3a_1)\mathbf{i} - (7\pi/3a_1)\mathbf{j}$. The wave number at resonance is $k = 5\sqrt{2}\pi/3a_1$.

are weak, and transmission is nearly complete. Within the ranges $-2.2 < \Omega/\Omega_0 < 1.8$ and $1.0 < \Omega/\Omega_0 < 1.45$, the decaying component $C_1 V_1^{(1)} \exp(i\lambda_1\Omega_0 X/C_g)$ is dominant from Fig. 25 and the transmission intensity $|B_1(L)|^2$ decreases rapidly in X. Meanwhile, both $|B_2(0)|^2$ and $|B_3(L)|^2$ increase significantly in accordance with the law of energy conservation (122).

D. Type III: Backward-backward scattering

Again we choose a square lattice of spacing a_1. The Ewald circle passing three nodes P_1, P_2, and P_3 in the reciprocal lattice is plotted in Fig. 28, where $\overrightarrow{P_1P_2} = \mathbf{K}_{-2,-1}$ and $\overrightarrow{P_1P_3} = \mathbf{K}_{-1,-2}$. The coordinates of the center S of the Ewald circle can be found by solving $|\overrightarrow{SP_1}| = |\overrightarrow{SP_2}| = |\overrightarrow{SP_3}|$, where the nodes P_1, P_2, P_3 are located at $\mathbf{b}_1 + \mathbf{b}_2$, $-\mathbf{b}_1$, $-\mathbf{b}_2$, respectively. The coordinates of the center S are found to be $\overrightarrow{OS} = (\pi\mathbf{i}/3a_1, \pi\mathbf{j}/3a_1)$. Hence the modulus of the wave number at resonance is

$$k = |\overrightarrow{SP_1}| = \sqrt{\left(\frac{2\pi}{a_1} - \frac{\pi}{3a_1}\right)^2 + \left(\frac{2\pi}{a_1} - \frac{\pi}{3a_1}\right)^2} = \frac{5\sqrt{2}\pi}{3a_1}. \tag{130}$$

The corresponding angles of $\mathbf{k}_1$, $\mathbf{k}_2$, and $\mathbf{k}_3$ are

$$\beta_1 = \arg(\overrightarrow{SP_1}) = \frac{\pi}{4} = 45°, \tag{131a}$$

$$\beta_2 = \arg(\overrightarrow{SP_2}) = -\pi + \tan^{-1}\frac{1}{7} \approx 171.87°, \tag{131b}$$

$$\beta_3 = \arg(\overrightarrow{SP_3}) = -\frac{\pi}{2} - \tan^{-1}\frac{1}{7} \approx -98.13°. \tag{131c}$$

Both $\mathbf{k}_2$ and $\mathbf{k}_3$ are backward.

As shown in Fig. 29 calculated from Eq. (117), the discriminant Δ_3 is mostly positive when the detuning Ω/Ω_0 is between -2.63 and 1.59, where one eigenvalue is real and two are complex conjugates. There is a narrow range $-0.9578 < \Omega/\Omega_0 < -0.9543$ where Δ_3 is negative and all three eigenvalues are real. The corresponding eigenvalues are plotted in Fig. 30.

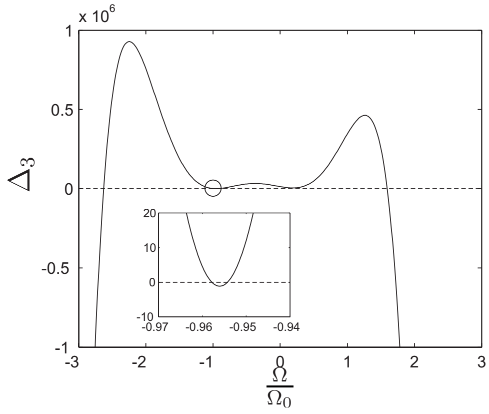

FIG. 29. Discriminant (117) for type III backward-backward Bragg scattering in Fig. 28.

After applying the boundary conditions (121), the coefficients C_1, C_2, C_3 are found:

$$\begin{bmatrix} C_1 \\ C_2 \\ C_3 \end{bmatrix} = \frac{\begin{bmatrix} e^{i(\lambda_2+\lambda_3)\Omega_0 L/C_g}(V_2^{(2)}V_3^{(3)} - V_2^{(3)}V_3^{(2)}) \\ e^{i(\lambda_1+\lambda_3)\Omega_0 L/C_g}(V_2^{(3)}V_3^{(1)} - V_2^{(1)}V_3^{(3)}) \\ e^{i(\lambda_1+\lambda_2)\Omega_0 L/C_g}(V_2^{(1)}V_3^{(2)} - V_2^{(2)}V_3^{(1)}) \end{bmatrix}}{\det\begin{bmatrix} V_1^{(1)} & V_1^{(2)} & V_1^{(3)} \\ e^{i\lambda_1\Omega_0 L/C_g}V_2^{(1)} & e^{i\lambda_2\Omega_0 L/C_g}V_2^{(2)} & e^{i\lambda_3\Omega_0 L/C_g}V_2^{(3)} \\ e^{i\lambda_1\Omega_0 L/C_g}V_3^{(1)} & e^{i\lambda_2\Omega_0 L/C_g}V_3^{(2)} & e^{i\lambda_3\Omega_0 L/C_g}V_3^{(3)} \end{bmatrix}}. \tag{132}$$

The moduli of the three coefficients of the transmitted wave are plotted in Fig. 31 against the detuning Ω/Ω_0. To the left (right) of the band gap, the component with coefficient $C_2V_1^{(2)}$ $(C_1V_1^{(1)})$ is dominant and close to one, which implies

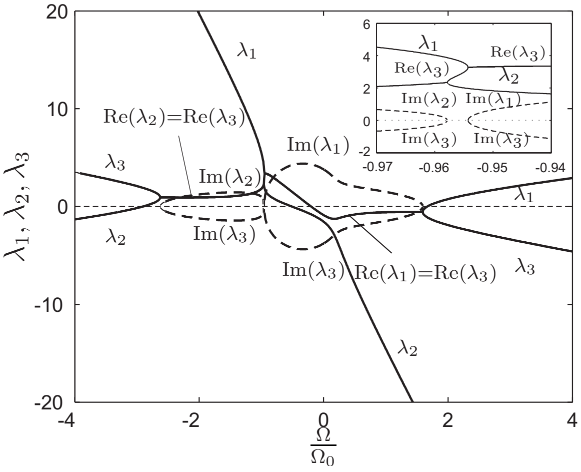

FIG. 30. Three eigenvalues for type III backward-backward Bragg scattering shown in Fig. 28. Solid curves are for the real parts and dashed curves are for the imaginary parts of eigenvalues.

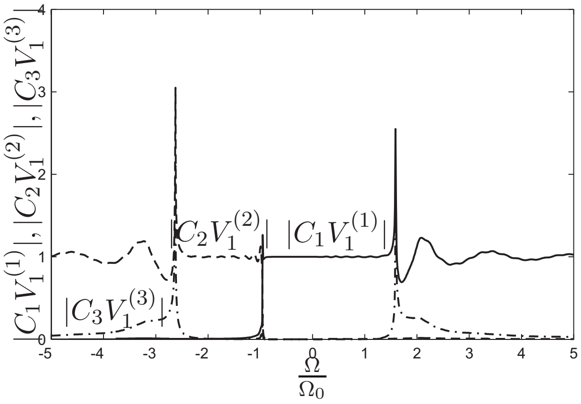

FIG. 31. Moduli of the three coefficients of the transmitted wave of a type III backward-backward three wave Bragg scattering shown in Fig. 28. Solid curve, $C_1V_1^{(1)}$; dashed curve, $C_2V_1^{(2)}$; dash-dot curve, $C_3V_1^{(3)}$.

that the transmission is nearly complete. Inside the band gap, the magnitude of the coefficient $C_3V_1^{(3)}$ for the oscillatory component is close to zero. Thus only the spatial attenuating component with the coefficient $C_2V_1^{(2)}$ is dominant when $-2.63<\Omega/\Omega_0<0.96$, and the component with coefficient $C_1V_1^{(1)}$ is dominant when $0.96<\Omega/\Omega_0<1.59$.

Figure 32 shows the spatial distribution of the transmission intensity $|B_1(X)|^2$ and the two reflection intensities $|B_2(X)|^2$, $|B_3(X)|^2$ across the strip of width $\Omega_0 L/C_g=2$. When $\Omega/\Omega_0=-4,-3,2,3$ (outside the band gap), reflection is weak and the transmitted wave propagates through the strip without significant attenuation. When $\Omega/\Omega_0=-2,-1,0,1$ (inside the band gap), the transmission intensity decay rapidly across the strip and reflection at the left edge of the strip is significant.

The dependence of the wave intensities on the detuning frequency is displayed for strip width $\Omega_0 L/C_g=2$ in Fig. 33. Outside the band gap, the intensities oscillate with Ω/Ω_0. Inside the band gap, transmission is nearly forbidden with $|B_1(L)|^2\approx 0$. Because $B_2(L)=B_3(L)=0$ according to the boundary conditions, nearly complete reflection is achieved. Furthermore, the two reflected waves on the incidence side of the strip are simply related by energy conservation,

$$\cos\beta_1|B_1(0)|^2+\cos\beta_2|B_2(0)|^2+\cos\beta_3|B_3(0)|^2 \\ =\cos\beta_1|B_1(L)|^2+\cos\beta_2|B_2(L)|^2+\cos\beta_3|B_3(L)|^2. \tag{133}$$

Using $|B_1(0)|^2=1$, $|B_1(L)|^2\approx 0$ and the values of β_j in Eqs. (131a)–(131c), we get

$$|B_3(0)|^2\approx 5-7|B_2(0)|^2. \tag{134}$$

We have performed calculations for a wider strip with $\Omega_0 L/C_g=5$. The results are similar, hence omitted.

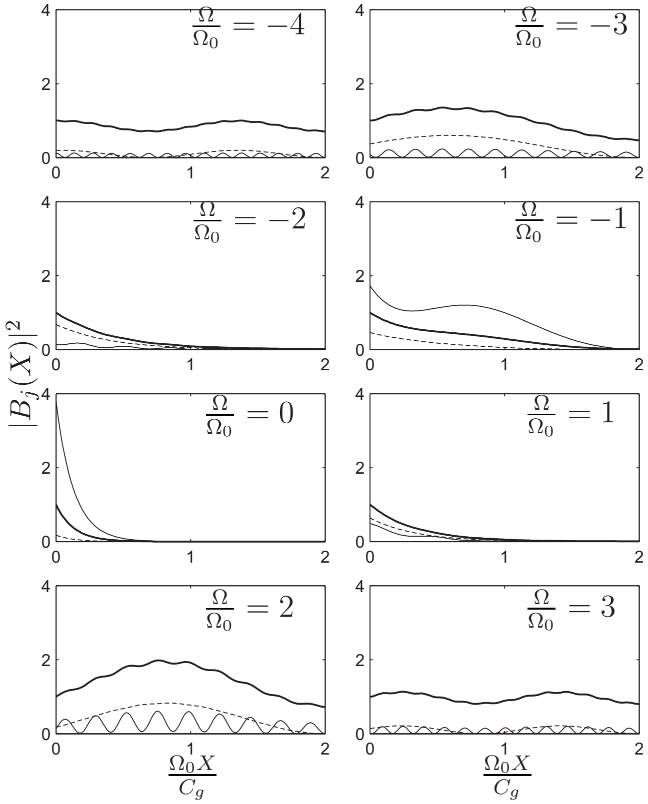

FIG. 32. Distribution of the wave intensities across the strip for various detuning frequency Ω/Ω_0. Type III scattering with $\Omega_0 L/C_g=2$. Thick solid curve, $|B_1(L)|^2$ (transmitted); dashed curve, $|B_2(X)|^2$ (reflected); thin solid curve, $|B_3(X)|^2$ (reflected). The reciprocal lattice and resonated wave vectors are shown in Fig. 28.

VIII. CONCLUDING REMARKS

We have developed an asymptotic theory for the two-dimensional scattering of infinitesimal water waves by a two-dimensional array of small cylinders in finite water depth. By the perturbation method of multiple scales, equations governing the evolution of the envelopes of N resonantly interacting waves are derived [see Eq. (43)]. The basic assumption is that the cylinder radius is much smaller than

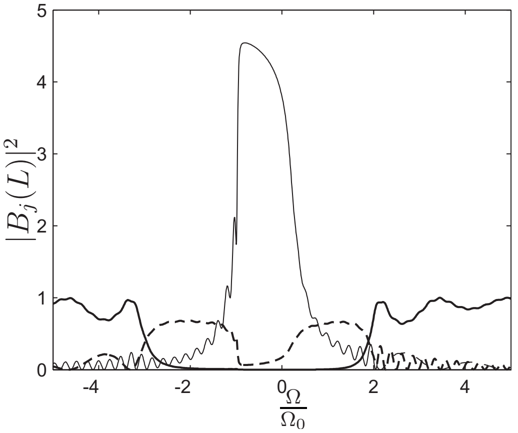

FIG. 33. Dependence of wave intensities on detuning frequency Ω/Ω_0 for type III scattering, with $\Omega_0 L/C_g=2$. Thick solid curve, $|B_1(L)|^2$ (transmitted); dashed curve, $|B_2(0)|^2$ (scattered); thin solid curve, $|B_3(0)|^2$ (scattered). The reciprocal lattice and resonated wave vectors are shown in Fig. 28.

either the incident wavelength or the cylinder spacing, i.e., $ka=\mu \ll 1$. From Bloch's condition and Ewald's construction, the number N of resonantly interacting waves increases with k, hence the present theory should be limited to moderate values of N for a given array and cylinder radius.

Analytical results are discussed for rectangular arrays forming a long strip of finite width, which may be an idealized model of one type of an offshore airport. A train of incident wave slightly detuned is assumed to arrive from one side of the strip. For two-wave resonance ($N=2$, one scattered wave), both forward- (e.g., Figs. 6 and 10) and backward-resonance (e.g., Fig. 11) are studied. For three-wave resonance ($N=3$, two scattered waves) possible configurations include forward-forward (e.g., Fig. 16), forward-backward (e.g., Fig. 22) and backward-backward scattering (e.g., Fig. 28). Numerical results are calculated from the analytical formulas to illustrate the effects of detuning of the incident waves in and outside the band gap.

The analytical method here can be applied to two-dimensional sound waves in air, or SH elastic waves, with minor modifications. In addition to facilitating physical understanding, the present asymptotic theory is more efficient and accurate for more scatterers, unlike numerical approaches. If the region of the cylinder array is not bounded by parallel straight lines, the envelope problem involves two-dimensional diffraction in the slow coordinate. For a circular domain, analytical solution is feasible. For a more general domain numerical tools are needed to solve the coupled-mode equations.

For ocean engineering applications, the additional effects of vortex shedding around small cylinders must be accounted for in the future, not only for better modeling of the wave forces but for the variation of wave amplitudes in the region of scatterers. This would be comparable to but different from the viscous dissipation in boundary layers around an array of large and truncated cylinders described in [46]. In addition, long waves and drift forces, induced by long groups of short incident waves, are second-order nonlinear effects of important concern to the design of potential offshore airports resting on piles. These effects require extensions which will be reported elsewhere.

ACKNOWLEDGMENTS

We acknowledge with gratitude the financial support by US Navy, Office of Naval Research (Grant No. N00014-04-1-0077), US National Science Foundation (Grant No. CTS 007573), and US-Israel Bi-National Science Foundation. Discussions with Jian Zi, Department of Physics, Fudan University, Shanghai, China, partly stimulated the present study. We also thank Dr. Ali Tabaei for a careful reading of our manuscript.

APPENDIX A: AN INTEGRAL IDENTITY

As shown in Fig. 34, the unit cell area $\mathcal{A}=\mathcal{A}_F+\pi a^2$ in (x,y) coordinates can be mapped onto a unit square in (ξ_1,ξ_2) by

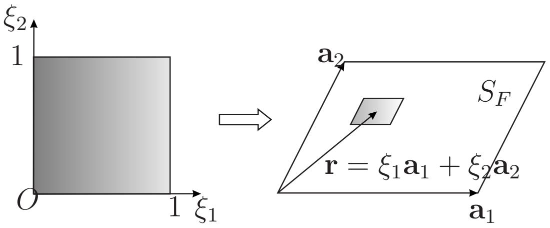

FIG. 34. Mapping from a unit square in (ξ_1,ξ_2) toward the unit cell in (x,y).

$$\mathbf{r}(x,y)=\xi_1\mathbf{a}_1+\xi_2\mathbf{a}_2. \tag{A1}$$

Thus the integral over $\mathcal{A}$ on the right side of Eq. (35) becomes

$$\int\int_{\mathcal{A}} e^{i(\mathbf{k}_h-\mathbf{k}_j)\cdot\mathbf{r}}dS=|\mathbf{a}_1\times\mathbf{a}_2|\int_0^1 d\xi_1\int_0^1 d\xi_2 e^{i(\mathbf{k}_h-\mathbf{k}_j)\cdot(\xi_1\mathbf{a}_1+\xi_2\mathbf{a}_2)}. \tag{A2}$$

Making use of the Bragg resonance condition (6) and noting that $\mathcal{A}=|\mathbf{a}_1\times\mathbf{a}_2|$, the above integral becomes

$$\begin{aligned}\int\int_{\mathcal{A}} e^{i(\mathbf{k}_h-\mathbf{k}_j)\cdot\mathbf{r}}dS&=\mathcal{A}\int_0^1\int_0^1 e^{i\mathbf{K}_{j,h}\cdot(\xi_1\mathbf{a}_1+\xi_2\mathbf{a}_2)}d\xi_1 d\xi_2\\&=\mathcal{A}\int_0^1 e^{i\xi_1(\mathbf{K}_{j,h}\cdot\mathbf{a}_1)}d\xi_1\int_0^1 e^{i\xi_2(\mathbf{K}_{j,h}\cdot\mathbf{a}_2)}d\xi_2.\end{aligned} \tag{A3}$$

The single integral in Eq. (A3) can be calculated

$$\int_0^1 e^{i\xi_n(\mathbf{K}_{j,h}\cdot\mathbf{a}_n)}d\xi_n=\begin{cases}\dfrac{e^{i(\mathbf{K}_{j,h}\cdot\mathbf{a}_n)}-1}{i\mathbf{K}_{j,h}\cdot\mathbf{a}_n}, & j\neq h,\\ 1, & j=h,\end{cases}\qquad \text{for } n=1,2. \tag{A4}$$

Making use of the identity $e^{i\mathbf{K}_{j,h}\cdot\mathbf{a}_n}=1$ in Eq. (4), the above integral on the left becomes

$$\int_0^1 e^{i\xi_n(\mathbf{K}_{j,h}\cdot\mathbf{a}_n)}d\xi_n=\delta_{jh},\qquad n=1,2, \tag{A5}$$

where δ_{jh} is the Kronecker delta. Finally, the integral (A3) becomes

$$\int\int_{\mathcal{A}} e^{i(\mathbf{k}_h-\mathbf{k}_j)\cdot\mathbf{r}}dS=(\delta_{jh})^2\mathcal{A}=\delta_{jh}\mathcal{A}. \tag{A6}$$

APPENDIX B: EVALUATION OF COEFFICIENTS

To evaluate the surface integral over the circular cylinder S_B,

$$I_B=-\int\int_{S_B}\left(\phi_2\frac{\partial\psi_j^*}{\partial\rho}-\psi_j^*\frac{\partial\phi_2}{\partial\rho}\right)dS, \tag{B1}$$

use must be made of the inner approximations ϕ_2^{in} for ϕ_2, i.e., Eqs. (31) and (29). On the cylinder surface $\rho=a$, we get

$$\begin{aligned}\psi_j^*\big|_{\rho=a} &= Z(z)e^{-i\mathbf{k}_j\cdot(\mathbf{r}'+\mathbf{R})}\big|_{\rho=a}\\ &= Z(z)e^{-i\mathbf{k}_j\cdot\mathbf{R}}[1-ika\cos(\varphi-\beta_j)+O(\mu^2)]\end{aligned}\tag{B2}$$

and

$$\left.\frac{\partial\psi_j^*}{\partial\rho}\right|_{\rho=a} = Z(z)[-ik\cos(\varphi-\beta_j)]e^{-i\mathbf{k}_j\cdot(\mathbf{r}'+\mathbf{R})}\big|_{\rho=a} = Z(z)e^{-i\mathbf{k}_j\cdot\mathbf{R}}[-ik\cos(\varphi-\beta_j)][1+O(\mu)].\tag{B3}$$

With the help of Eqs. (31) and (B3), we first calculate the surface integral of $\phi_2(\partial\psi_j^*/\partial\rho)$

$$\begin{aligned}\int\int_{S_B}\phi_2\frac{\partial\psi_j^*}{\partial\rho}dS &= \int_{-H}^{0}dz\int_0^{2\pi}\phi_2^{\text{in}}\frac{\partial\psi_j^*}{\partial\rho}a\,d\varphi\\ &= \int_{-H}^{0}Z^2(z)dz\sum_{h=1}^{N}\left\{A_he^{i(\mathbf{k}_h-\mathbf{k}_j)\cdot\mathbf{R}_{m_1,m_2}}\int_0^{2\pi}\left[\frac{ka}{\mu}\cos(\varphi-\beta_h)\cos(\varphi-\beta_j)-\frac{ika}{2}\ln\mu\cos(\varphi-\beta_j)+O(ka)\right]d\varphi\right\}\\ &= \sum_{h=1}^{N}\pi A_h\cos(\beta_j-\beta_h)\int_{-H}^{0}Z^2(z)dz+O(\mu).\end{aligned}\tag{B4}$$

Use is made of the identities $ka=\mu$, $\int_0^{2\pi}\cos(\varphi-\beta_j)\cos(\varphi-\beta_h)d\varphi=\pi\cos(\beta_j-\beta_h)$, $\int_0^{2\pi}\cos(\varphi-\beta_j)d\varphi=0$, and $e^{i(\mathbf{k}_j-\mathbf{k}_h)\cdot\mathbf{R}}=e^{i\mathbf{K}_{j,h}\cdot\mathbf{R}}=1$. Next we calculate the surface integral of $\psi_j^*(\partial\phi_2/\partial\rho)$ over S_B, by using Eqs. (29) and (B2),

$$\begin{aligned}\int\int_{S_B}\psi_j^*\frac{\partial\phi_2}{\partial\rho}dS &= \int\int_{S_B}\psi_j^*\frac{\partial\phi_2^{\text{in}}}{\partial\rho}dS\\ &= -\sum_{h=1}^{N}kaA_he^{i(\mathbf{k}_h-\mathbf{k}_j)\cdot\mathbf{R}_{m_1,m_2}}\int_{-H}^{0}Z^2(z)dz\int_0^{2\pi}[1-ika\cos(\varphi-\beta_j)+O(\mu^2)]\\ &\quad\times\left(\frac{i\cos(\varphi-\beta_h)}{\mu^2}-\frac{1+\cos2(\varphi-\beta_h)}{2\mu}+O(1)\right)d\varphi\\ &= -\sum_{h=1}^{N}A_h\int_{-H}^{0}Z^2(z)dz\int_0^{2\pi}d\varphi\left(\frac{i\cos(\varphi-\beta_h)}{\mu}-\frac{1+\cos2(\varphi-\beta_h)}{2}+\cos(\varphi-\beta_j)\cos(\varphi-\beta_h)+O(\mu)\right)\\ &= -\sum_{h=1}^{N}\pi A_h[-1+\cos(\beta_j-\beta_h)]\int_{-H}^{0}Z^2(z)dz+O(\mu),\end{aligned}\tag{B5}$$

where use is made of the identity $\int_0^{2\pi}\cos2(\varphi-\beta_h)d\varphi=0$.

Substituting Eqs. (B4) and (B5) into Eq. (B1), the surface integral on the cylinder becomes Eq. (38).

[1] J. Wilson, Popular Mechanics **180**, 92 (2003).
[2] B. E. Warren, *X-ray Diffraction* (Addison-Wesley, Redwood City, CA, 1969).
[3] C. Kittel, *Introduction to Solid State Physics*, 8th ed. (Wiley, New York, 2004).
[4] N. W. Aschcroft and N. D. Mermin, *Solid State Physics* (Holt, Rhinehart, and Winston, New York, 1976).
[5] A. Yariv and P. Yeh, *Optical Waves in Crystals: Propagation and Control of Laser Radiation* (Wiley-Interscience, New York, 1984).
[6] J. D. Joannopoulos, R. D. Meade, and J. N. Winn, *Photonic Crystals: Molding the Flow of Light* (Princeton University Press, Princeton, NJ, 1995).
[7] D. V. Evans and R. Porter, J. Fluid Mech. **339**, 331 (1997).
[8] D. V. Evans and R. Porter, J. Eng. Math. **35**, 149 (1999).
[9] P. McIver, J. Fluid Mech. **424**, 101 (2000).
[10] T. Chou, J. Fluid Mech. **369**, 333 (1998).
[11] X. Hu, Y. Shen, X. Liu, R. Fu, J. Zi, X. Jiang, and S. Feng, Phys. Rev. E **68**, 037301 (2003).
[12] X. Hu, Y. Shen, X. Liu, R. Fu, and J. Zi, Phys. Rev. E **68**, 066308 (2003).
[13] P. Yeh, *Optical Waves in Layered Media* (Wiley, New York, 1988).
[14] S.-L. Chang, *X-Ray Multiple-Wave Diffraction: Theory and Application* (Springer-Verlag, Berlin, 2004).
[15] D. Maystre, M. Saillard, and G. Tayeb, in *Scattering*, edited by P. Sabatier and E. R. Pike (Academic, London, 2001).
[16] H. Kagemoto and D. K. P. Yue, J. Fluid Mech. **166**, 189 (1986).
[17] P. McIver, Appl. Ocean. Res. **24**, 121 (2002).

[18] C. M. Linton and D. V. Evans, J. Fluid Mech. **215**, 549 (1990).
[19] M. A. Peter and M. H. Meylan, J. Fluid Mech. **500**, 145 (2004).
[20] M. A. Peter, M. H. Meylan, and C. M. Linton, J. Fluid Mech. **548**, 237 (2006).
[21] C. M. Linton and D. V. Evans, *Handbook of Mathematical Techniques for Wave/Structure Interactions* (Chapman & Hall/CRC, Boca Raton, FL, 2001).
[22] P. Martin, *Multiple Scattering: Interaction of Time-Harmonic Waves with N Obstacles* (Cambridge University Press, Cambridge, UK, 2006).
[23] M. Ohkusu, Rep. Res. Inst. Appl. Mech. (Kyushu Univ.) **58**, 167 (1970).
[24] M. A. Srokosz and D. V. Evans, J. Fluid Mech. **90**, 337 (1979).
[25] D. V. Evans, J. Fluid Mech. **210**, 647 (1990).
[26] X. Hu and C. T. Chan, Phys. Rev. Lett. **95**, 154501 (2005).
[27] Y. Tang, Y. Shen, J. Yang, X. Liu, J. Zi, and X. Hu, Phys. Rev. E **73**, 035302(R) (2006).
[28] X. Hu, Y. Shen, X. Liu, R. Fu, and J. Zi, Phys. Rev. E **69**, 030201(R) (2004).
[29] Y. Shen, K. Chen, Y. Chen, X. Liu, and J. Zi, Phys. Rev. E **71**, 036301 (2005).
[30] R. Slusher and B. J. Eggleton, *Nonlinear Photonic Crystals* (Springer, Berlin, 2003).
[31] A. A. Barybin and V. A. Dmitriev, *Modern Electrodynamics and Coupled-Mode Theory: Application to Guided-Wave Optics* (Rintlon, Princeton, NJ, 2002).
[32] C. C. Mei, J. Fluid Mech. **152**, 315 (1985).
[33] T. Hara and C. C. Mei, J. Fluid Mech. **178**, 221 (1987).
[34] C. C. Mei, T. Hara, and M. Naciri, J. Fluid Mech. **186**, 147 (1988).
[35] V. Rey, E. Guazzelli, and C. C. Mei, Phys. Fluids **8**, 1525 (1996).
[36] M. Naciri and C. C. Mei, J. Fluid Mech. **192**, 51 (1988).
[37] R. Goodman, M. I. Weinstein, and P. J. Holmes, J. Nonlinear Sci. **11**, 123 (2001).
[38] J. W. S. Rayleigh, Philos. Mag. **12**, 81 (1881).
[39] Y. Li, Ph.D. thesis, Massachusetts Institute of Technology, 2006 (unpublished).
[40] Y. Li and C. C. Mei, J. Fluid Mech. **583**, 161 (2007).
[41] C. C. Mei, M. Stiassnie, and D. K. P. Yue, *Theory and Applications of Ocean Surface Waves* (World Scientific, Singapore, 2005).
[42] J. B. Pendry and D. R. Smith, Phys. Today **57** (6), 37 (2004).
[43] A. Authier, *Dynamical Theory of X-ray Diffraction* (Oxford University Press, New York, 2001), p. 661.
[44] G. N. Watson, *A Treatise on the Theory of Bessel Functions* (Cambridge University Press, Cambridge, UK, 1941).
[45] M. Abramowitz and I. A. Stegun, *Handbook of Mathematical Functions* (Dover, New York, 1972).
[46] H. Kagemoto, M. Murai, M. Saito, B. Molin, and S. Malenica, J. Fluid Mech. **456**, 113 (2002).
[47] In this article, the first index $j=1$ is reserved for the incident wave.